Colour-Magnitude Diagrams of Transiting Exoplanets

by

Georgina Dransfield

A thesis submitted to the

University of Birmingham

for the degree of

MASTER OF SCIENCE

Sun, Stars and Exoplanets

School of Physics and Astronomy

University of Birmingham

Birmingham, B15 2TT

February 2020

UNIVERSITY OF BIRMINGHAM

University of Birmingham Research Archive

e-theses repository

Abstract

Colour-Magnitude Diagrams provide a simple way of comparing populations of similar objects; and when well populated with precise measurements they allow quick inferences to be made about the bulk properties of an astronomic object simply from its proximity on a diagram to other objects. We present here a Python toolkit which allows a user to produce colour-magnitude diagrams of transiting exoplanets, comparing planets to populations of ultra-cool dwarfs and directly imaged exoplanets, to models of planetary atmospheres, and to other transiting exoplanets. Using a selection of near- and mid-infrared colour-magnitude diagrams, we show how outliers can be identified for further investigation, and how emerging sub-populations can be identified. Additionally, we present evidence that observed differences in the *Spitzer*'s 4.5μm flux, between irradiated Jupiters, and field field brown dwarfs, might be attributed to Phosphine, which is susceptible to photolysis. If confirmed, this may negate the need for thermal inversions to explain eclipse measurements. We extend this reasoning to other objects and speculate that the anomalously low 4.5μm flux flux of the nightside of HD 189733b and the daysides of GJ 436b and GJ 3470b might be caused by Phosphine absorption. Finally, we use our toolkit to include *Hubble* WFC3 spectra, creating a new photometric band called the 'Water band' (W_{JH}-band) in the process. We show that the colour index [W_{JH}-H] can be used to constrain the C/O ratio of exoplanets, showing that future observations with *JWST* and *ARIEL* will be able to distinguish these populations if they exist, and select members for future follow-up.

The work presented in this thesis is being prepared for publication in a paper on which I will be first author. The abstract above is lifted verbatim from the current manuscript of that paper.

Dedication

This work is dedicated to Ian and Amy, both of whom care very deeply about science.

Acknowledgements

Contents

List of Figures

List of Tables

Structure of Thesis

This thesis is comprised of five chapters. The first chapter presents a brief introduction to the current state of the field of exoplanets, focusing in particular on the areas of research pertinent to this work. In the second chapter, I outline the methods employed in the assembly of the database, as well as the processing of the data.

Chapter 3 presents colour-magnitude diagrams in near- and mid-infrared bands, and describes all the inferences we have been able to draw from these plots. I discuss the significance of these results in the context of the field in Chapter 4 and conclude in Chapter 5.

Within each chapter, there are large sections drawn verbatim from a paper currently in preparation on which I will be first author. This is particularly the case in Chapters 3 and 4.

1   INTRODUCTION

The vast majority of this chapter was written for this thesis, as significantly more context is given here than would be needed in a journal paper. However, Sections 1.3 and 1.4 is lifted almost verbatim from a paper in preparation in which I will be first author.

1.1   The search for exoplanets begins

To many readers it may come as a surprise to learn that there were claims of a planet outside the solar system about 85 years before Pluto was discovered (Leonard, 1930), and only nine years after the discovery of Neptune (Galle, 1846): in 1855 Captain W.S. Jacob proposed the existence of a circumbinary exoplanet to resolve irregularities in the positions of the 70 Ophiuchi stars (Jacob, 1855). This was later refuted by Moulton 1899, and from then we had to wait almost a century until the first confirmed exoplanets were discovered by Wolszczan & Frail (1992).

While PSR B1257+12 B and C were the first two planets discovered, their discovery method of pulsar timing has only yielded a handful planets since (for a detailed review, see: Hermes, 2018). There are now several methods of exoplanetary detection, each lending itself to a particular type of system. Microlensing for instance, allows us to detect very distant planets close to the centre of the galaxy; this is because the planet and its parent star will bend the light of an even more distant star, causing the observed light to appear blurred (for a review: Batista, 2018). When detecting planets via radial velocity measurements however, we rely on the periodic Doppler shifting of the host star's spectral lines, caused by its motion around the common centre of mass as it is orbited by a planet (e.g. Lovis & Fischer, 2010; Wright, 2018).

In Figure 1.1 we present a plot showing exoplanet masses vs their semi-major axes, with each system coloured according to its discovery method. We can see that radial velocities and
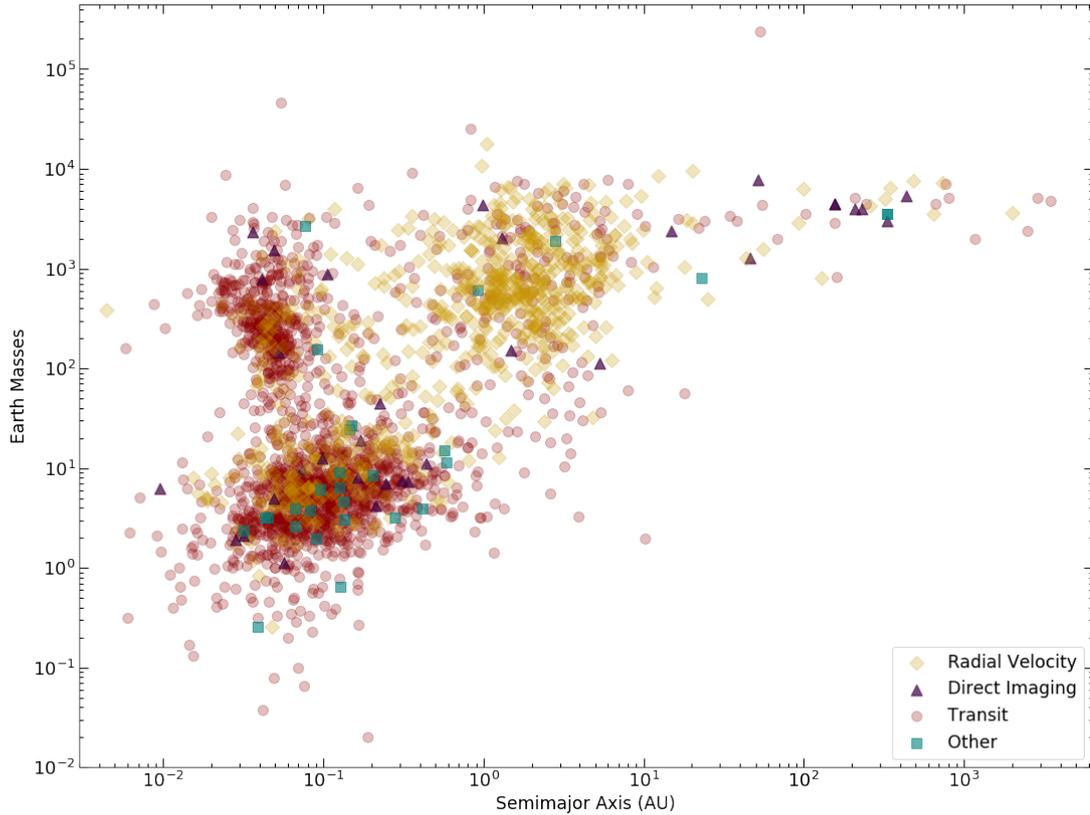
Figure 1.1: Exoplanetary masses as a function of their orbital separations. Each system has been coloured according to its discovery method. Plot compiled with data provided by the NASA Exoplanet Archive.

transits have yielded the most systems, accounting for over 3500 planets between them.

In the following sections we will introduce the two principal methods of exoplanetary detection which are pertinent to this work. While radial velocitiy measurements has led to significantly more discoveries than direct imaging, a detailed explanation of this mechanism is beyond the scope of this work to explain.

1.1.1 Transits as a discovery method

When a planet passes in front of its star during a primary eclipse event, if the orientation of the system is favourable we will observe a transit. A transit results in a dip in the flux of the parent star as its disk is partially obscured by the transiting planet. In this way we can detect a planet, even if it is not spatially resolved, from its effect on the light of the star.

The first planet to have its transit detected was HD 209458b (Charbonneau et al., 2000), although it had already been discovered via radial velocity measurements by Henry et al. (1999).

The first planet to be *discovered* via transit observations was OGLE-TR-56b (Konacki et al., 2003).

There have now been several thousand planets detected in this way but as mentioned above, a favourable geometric alignment is required for a transit to be observed from Earth. Winn (2010) gives the transit probability as:

$$p_{transit} = \left(\frac{R_\star + R_p}{a \left(1 - e^2 \right)} \right) \tag{1.1}$$

Where $R_\star$ is the radius of the star, R_p is the planetary radius, a is the semi-major axis, and e is the eccentricity of the orbit. In cases where the radius of the planet is negligible compared with the stellar radius, the equation reduces to:

$$p_{transit} = \left(\frac{R_\star}{a \left(1 - e^2 \right)} \right) \tag{1.2}$$

We can see from this that the probability is highest for objects orbiting very close to their parent stars. We can also deduce that we are more likely to observe a transit in a system with higher eccentricity. This leads to a selection bias as visualised in Figure 1.1: there are considerably more red points for orbital separations < 1AU.

1.1.2 Detecting planets via direct imaging

Over the last 10 years, there have approximately fifty planets detected by direct imaging[1], with orbital separations of up to 3500AU (Chinchilla et al., 2020).

Direct imaging is only possible for a select few systems; most planets cannot be spatially resolved due to their proximity to their host star and their comparative small size and dimness. It follows therefore that the systems that have been detected in this way contain exceptionally large planets on very wide orbits (Biller & Bonnefoy, 2018). Additionally, young planetary systems are favoured as the planets themselves are likely to be hotter and therefore emitting more infrared flux of their own (Traub & Oppenheimer, 2010).

In the visible, any flux detected from the planet is likely to be reflected from the star; therefore

---

[1]https://exoplanetarchive.ipac.caltech.edu/cgi-bin/TblView/nph-tblView?app=ExoTblsconfig=compositepars

the spectrum would be a lower intensity copy of the stellar spectrum. Nevertheless, this can allow determination of the geometric albedo of the system. In the infrared, we can expect to detect thermal emission from the planet itself, along with reprocessed stellar flux (Wright & Gaudi, 2013). This latter enables us to determine the planetary bond albedo.

While direct imaging is not without its challenges, once planets have been resolved it is possible to characterise their atmospheres by performing spectroscopic measurements on them. One of the best characterised systems in this way is the multi-planet HR8799 system (Marois et al., 2008); on discovery several near-infrared flux measurements were published which allowed charaterisation of the three planets before their radii and masses were even known.

1.2   Populations of exoplanets

The frequency of planetary discoveries we now enjoy indicates that they are fairly ubiquitous: planets are the norm rather than the exception. With so many planets now catalogued, there has been considerable effort put into the question of how to classify them.

One recent classification scheme used a data-driven model to classify planets based on their masses (Chen & Kipping, 2017). In Figure 1.2 we present a plot similar to Figure 10 presented in Chen & Kipping (2017); here we see the mass-radius relation for exoplanets and how this relation varies for the different categories of planet. In our plot we have included all planetary data currently available from the NASA Exoplanet Archive[2], whereas in the original plot only the 316 planets used to compute the model were included. We can see that there is a grouping of blue 'Jupiter-like' planets which sit significantly below the general trend, indicating they are smaller than other planets in this mass regime. Nevertheless, this classification scheme is intuitive as it derives from two of the most easily measured parameters for exoplanets.

A sub-category of Jovian (or Jupiter-like) worlds are the so-called hot Jupiters. These are gas giants that orbit very close to their parent stars and as such are highly inflated, reaching temperatures of up to 2500K (Hebb et al., 2009). These type of planets are thought to have occurrence rates of between 0.5-1% (Mordasini, 2018), but they are over-represented in surveys

---

[2]https://exoplanetarchive.ipac.caltech.edu/cgi-bin/TblView/nph-tblView?app=ExoTblsconfig=compositepars
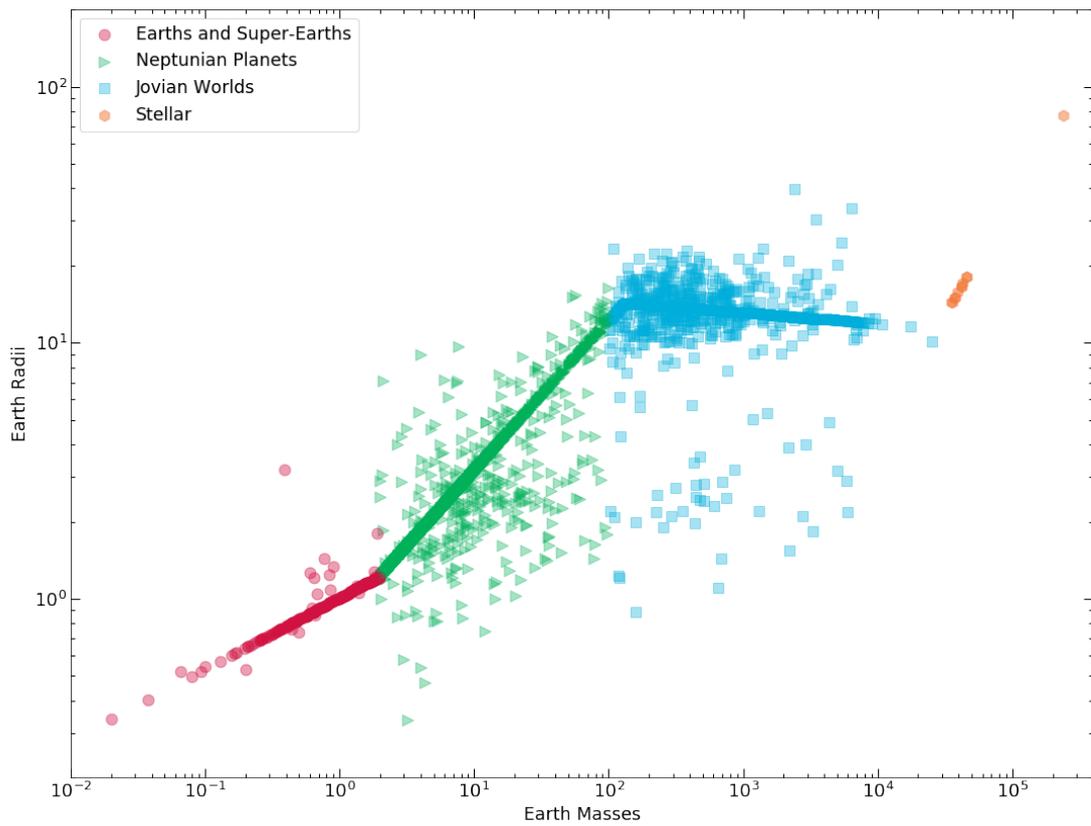
Figure 1.2: Exoplanet masses as a function of their radii. Each system has been coloured according to the classification scheme first published in Chen & Kipping (2017). Plot compiled with data provided by the NASA Exoplanet Archive.

as their large radii and short orbits make them easy for us to detect.

The discovery of the first hot Jupiter by Mayor & Queloz (1995) came as a big surprise: with an orbital period of just four days, it was understood that such a planet could not have formed in situ. In fact, the wisdom at the time stated that giant planets like Jupiter should form by the core-accretion method beyond the snowline (Pollack et al., 1996). In order to overcome this challenge, new models of giant planet formation were developed which allowed for the planet to form at larger orbital distances and then migrate inwards (Lin et al., 1996). However, more recently theories for in situ formation of hot Jupiters have come to light (Batygin et al., 2016) meaning that there is still controversy surrounding the origins of these objects. For a review of migration theories: (Baruteau & Masset, 2013), and for a review of giant planetary formation: (D'Angelo & Lissauer, 2018)

1.3   Further questions arise

As the scope of the field of exoplanets has broadened, so too has our ambition: we are now not content to simply know of a system's geometry, but are probing various layers of exoplanetary atmospheres through transit spectroscopy and multi-waveband photometry (for a review: Madhusudhan, 2019).

We are able to infer the presence of atomic (e.g. Charbonneau et al., 2002; Redfield et al., 2008) and molecular species (e.g. McCullough et al., 2014; Kreidberg et al., 2014; Sheppard et al., 2017). This in turn reveals some of the chemical and thermal transport processes taking place at different pressure levels within the atmosphere (Stevenson et al., 2014a). A clearer picture of the chemical composition of a planet's atmosphere allows us to compute useful parameters such as the carbon-to-oxygen (C/O) ratio (Moses et al., 2013a). The C/O ratio is particularly useful to probe the nebular gas in which the planet formed, and hence the location of its formation within a protoplanetary disc (Öberg et al., 2011; Madhusudhan et al., 2011b).

One of the key strategies employed is to observe the combined light of the star and exoplanet. In particular, transmission spectroscopy can be performed during a transit as the light from the star passes through the planetary atmosphere.
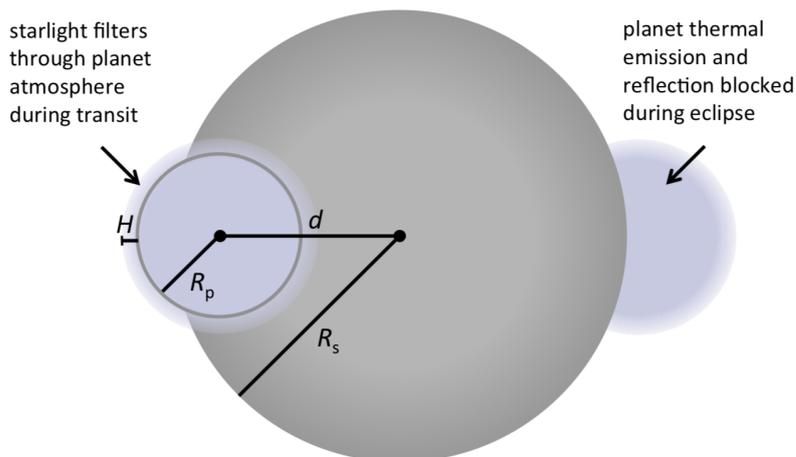
Figure 1.3: Geometry of primary and secondary eclipses, showing the region of the planet's atmosphere which can be characterised during each event. R_s is the stellar radius while R_p is the radius of the planet. H is the atmospheric scale height and d is the separation of the centres of the two objects, as viewed in the plane of the sky. Figure reproduced from Kreidberg (2018)

Inferences for the C/O ratio have regularly been performed on transmission spectra (Pinhas et al., 2019). However transmission only probes a special location of the atmosphere of a tidally locked planet, its terminator, which might not be representative of the whole. In addition, transmission spectra can be strongly affected by opacity on the line of sight, with haze and clouds often masking important features (Sing et al., 2016). Furthermore transmission can be affected by stellar contamination (e.g. Jordán et al., 2013; Rackham et al., 2017).

A solution is to measure a planet's integrated dayside thermal emission, which is obtained during a secondary eclipse event (or occultation) when the planet passes behind its parent star (Kreidberg, 2018). When this has been detected in several photometric bands a low resolution emission spectrum emerges (Alonso, 2018), which we can use to retrieve atmospheric compositions. Figure 1.3 details the relative arrangement of planet and star during the transit and occultation, highlighting which parts of the atmosphere are visible during each.

The process of atmospheric retrieval relies on reliable atmospheric models, which require accurate chemical networks and complete line lists for all the main opacity sources (see Madhusudhan (2018) for a detailed review of atmospheric retrieval processes). At present we have access to several state-of-the-art modelling codes, but they are very much still in flux, with chemical networks and line lists being updated frequently (e.g. Baudino et al., 2017; Venot et al.,

7

2019; Hobbs et al., 2019). Retrieval codes being computationally intensive, there is interest in including as small a number of species as possible. However if a certain molecule is present in the atmosphere, but absent in the code, the retrieved abundances will be inaccurate (Waldmann & Rocchetto, 2015; MacDonald & Madhusudhan, 2017). Obtaining diagnostics about which atomic or molecular species are present in a spectrum is therefore important. This is where colour-magnitude diagrams can help.

1.4 New avenues for H-R Diagrams

The field of exoplanet physics is in its infancy when compared to the field of stellar physics, and this latter hit a turning point with the plotting of the first Hertzsprung-Russell diagram (Hertzsprung, 1911; Russell, 1914). The H-R diagram was crucial as it allowed astronomers to statistically characterise a single object by placing it in the context of a well-studied population. In this way, sub-populations could be identified as well as their formation and evolution mechanisms (Eddington, 1920), allowing future observation strategies to be shaped.

We are now approaching a turning point in the field of exoplanetary observations: the launch of the James Webb Space Telescope (*JWST*), which is scheduled for March of 2021, will allow more detailed characterisation of planetary atmospheres than ever before (See Madhusudhan (2019), Figure 10). As such, it is vital that we exploit the data already available to select the very best targets for further investigation. Looking further into the future, the Atmospheric Remote-sensing Infrared Exoplanet Large-survey (*ARIEL*) is to be launched in 2028, with the goal of observing approximately 1000 planets to compile the planetary equivalent of an H-R Diagram (Encrenaz et al., 2018). While a Bolometric Luminosity vs. Spectral Type H-R diagram is is not yet achievable for planets, mid- and near-infrared colour-magnitude and colour-colour diagrams are already used in the field to help characterise atmospheres (Zhou et al., 2015; Kammer et al., 2015; Triaud et al., 2015; Alonso, 2018; Deming et al., 2019).

Direct imaging of exoplanets yields a straightforward measurement of the planet's brightness; for planets observed in this way, the use of a colour-magnitude diagram to compare it with objects of similar brightness is intuitive (e.g. Mohanty et al., 2007; Marois et al., 2008; Beatty et al.,

2014; Bowler, 2016). The use of colour-magnitude diagrams for *transiting* exoplanets was first seen in Triaud (2014), and later expanded on by Triaud et al. (2014). Colour-magnitude diagrams serve a similar purpose to H-R diagrams in that they allow for planets to be compared to a larger population. In the most recent paper in this series, distance measurements were photometrically estimated due to the lack of availability of parallaxes for most systems.

Colour-magnitude diagrams presented in Triaud et al. (2014) showed that in general the planets are compatible in magnitude with dwarfs of M and L spectral classes, although there is more diversity in colour shown by the exoplanets, most of which were hot Jupiters. In some bands, planets appeared to be equally compatible with blackbodies as they sat at the intersection of the two sequences. Manjavacas et al. (2019) also used a near-infrared colour-magnitude diagram to show that in J and H bands brown dwarfs are good spectral matches for hot Jupiters.

1.5 Widening the usage of colour-magnitude diagrams

While new secondary eclipse measurements are frequently published, it is still uncommon to see individual planets compared to entire populations on the basis of these measurements. With this in mind, there are two key aims set out in this thesis: the first aim is to develop a user-friendly Python toolkit that will enable members of the community to plot near- and mid-infrared colour-magnitude diagrams in order to view results in context. The second aim is to demonstrate the usefulness of this analysis technique, exemplified by a selection of newly plotted diagrams and the inferences that have derived from them.

This thesis is simply structured; in Chapter 2 we outline how the current dataset was assembled, and how the data is processed in the Python toolkit. Additionally, we present a walk-through of the interactive applet which will be available publicly for the exoplanet community. In Chapter 3 we present updated versions of colour-magnitude diagrams presented in Triaud et al. (2014), followed by a selection of new diagrams which have enabled us to delve deeper into systems which have been known about for several years. We discuss the significance of our findings in Chapter 4, placing them in the context of the current state of the field. Finally, we conclude in Chapter 5.

2   METHODS

In this chapter I have significantly expanded on the content of the methods section of a paper in preparation on which I will be first author. The sections lifted from the paper are placed in this chapter verbatim.

In this chapter, we describe the methods we have used to process spectra and secondary eclipse data found in the literature. We also outline the functionality of our Python modules, which we are making publicly available on an online repository in order to facilitate similar data handling by other astronomers.

We first describe how we have assembled our data-set and the data contained therein. We then explain how we processed spectra to produce our comparison samples in Section 2.3 along with our motivations for each choice. Finally, in section 2.6 we outline the functionality of the three modules which make up our Python toolkit, along with the interactive iPython applet we have developed for users.

2.1   Database of transiting exoplanet emission measurements

Our starting point was the data set compiled by Triaud et al. (2014). Since 2014, a handful of these measurements have been updated; additionally, there have been many secondary eclipses measured for the first time. Alonso (2018) provided a helpful list of planets with secondary eclipse measurements, together with the bands in which the data are available. Garhart et al. (2019) published secondary eclipses for 36 planets in *Spitzer*'s Channels 1 and 2, 27 of which had been measured for the first time. We also made use of the NASA Exoplanet Archive[1] which

---

[1] `https://exoplanetarchive.ipac.caltech.edu/cgi-bin/TblView/nph-tblView?app=ExoTbls&config=emissionspec`

provides secondary eclipse data in all bands, and we continuously searched the ADS and Arxiv for new publications containing planetary emissions. The keyword combinations we found most successful for these searches were 'exoplanet emission' and 'exoplanet secondary eclipse'. All of these resources allowed us to assemble an up-to-date database of fluxes measured at occultation for a sample of 83 exoplanets. While there are more systems with such measurements, for the purpose of this project only infrared fluxes were considered. Additionally, we did not include systems that only had measurements in a single band as at least two bands are needed for a colour index calculation.

Once our planet sample was assembled, we searched the 2MASS catalogue (Cutri et al., 2003) for host star apparent magnitudes in *J*, *H* and *K*-bands. As *Spitzer*'s IRAC instrument reached the end of its cryogenic lifetime before 2014, there have been no new measurements in the 5.8μm or 8μm channels. In order to obtain host star apparent magnitudes in the 3.6μm and 4.5μm channels, we made use of the *WISE* All-Sky catalogue (Cutri & et al., 2012) as WISE's channels W1 and W2 are very similar to *Spitzer*'s Channels 1 and 2. (Triaud et al., 2014).

Where a host star apparent magnitude was not available, we made use of standard spectra from the Pickles Atlas[2]. In order to calculate the magnitudes of the parent stars, we began by searching `exoplanet.eu` (Schneider et al., 2011) for the spectral type of the host star. We acquired the Pickles spectrum corresponding to the parent star's spectral type; we then integrated the flux in 2MASS *J*, *H* and *K* bands. For all magnitudes computed in this paper, we use the Vega-Magnitude system, setting its apparent magnitude to zero in all bands.

In order to compute Vega's flux in *J*, *H* and *K* we obtained Kurucz's high resolution spectrum[3] which we then integrated in all three bands. Finally, we recovered *H* and *K* magnitudes from *J*, *J* and *H* from *K*, and *J* and *K* from *H*. Where the spectral type of the parent star was not certain in the literature, we chose the spectrum which was a best fit in terms of temperature and recovered magnitudes. We present one-to-one plots of these recovered magnitudes in Figure 2.1.

To compute absolute magnitudes, we need distance with Gaia's DR2 providing the most

---
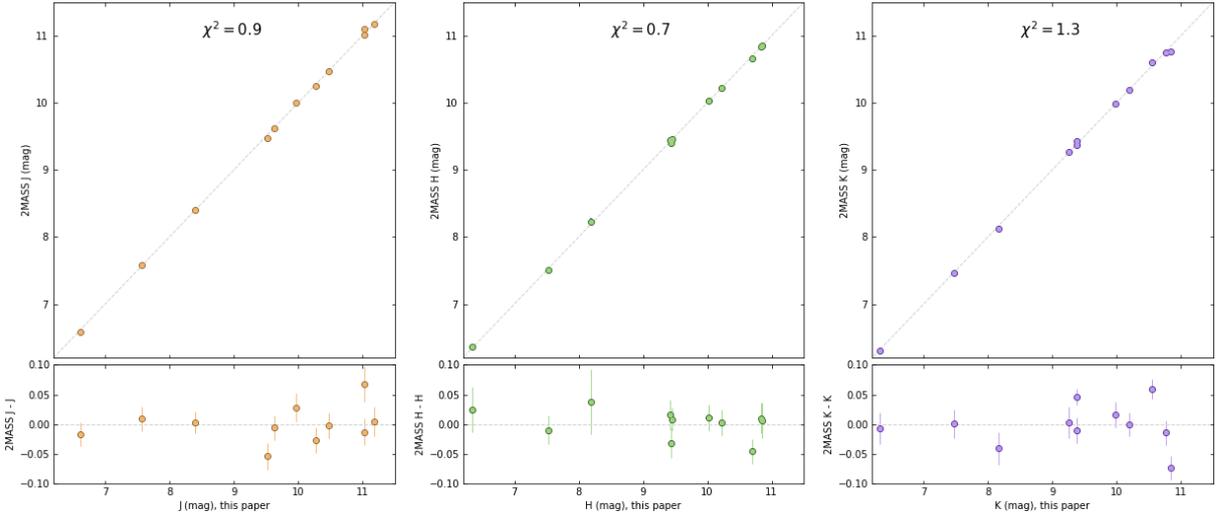
Figure 2.1: One-to-one plots of the 2MASS magnitudes of parent stars from the literature compared with our recovered mags using standard spectra from the Pickles Atlas. Residuals are shown in the lower three panels and the reduced χ^2 is given for each plot.

recent parallaxes (Gaia Collaboration et al., 2016, 2018). The distances could not be determined simply by inverting the parallaxes published in DR2 due to the non-linearity of the process of parallax estimation by Gaia; instead, we used the distances calculated by Bailer-Jones et al. (2018).

Finally the planetary radii were retrieved from `exoplanet.eu` (Schneider et al., 2011) and NASA Exoplanet Archive. Our compilation of planetary secondary eclipse measurements can be found in Appendix A

2.2 Transforming planetary flux into magnitudes

In order to add planets to a colour-magnitude diagram, we convert the fluxes measured at occultation to apparent magnitudes using the usual relation

$$m_p = -2.5 \times \log\left(\frac{F_p}{F_\star}\right) + m_\star \tag{2.1}$$

Where m_p is the apparent magnitude of the planet, $m_\star$ is the apparent magnitude of the parent star in the same band, and $F_p/F_\star$ is the planet-to-star flux ratio measured during the secondary eclipse event (Winn, 2010). These are then converted to absolute magnitudes using astrometric distances.

In addition, we integrate low resolution emission spectra measured with the G141 grism on the Wide Field Camera 3 instrument (WFC3) on board the *Hubble* Space Telescope to produce additional planetary photometry. This particular instrument covers the wavelength range 1.1–1.7μm which overlaps with the majority of the *J*-band. By cutting this grism between 1.130 and 1.325μm and integrating the planetary flux, we were able to compute short *J*-band photometry for eleven planets. The WFC3 grism extends into the *H*-band as well, but cuts short. We integrated the WFC3 spectra to create an *H*-short band, as was done in Manjavacas et al. (2019), however we do not include this photometry as the difference in magnitudes between the *H* and H_S exceeds the size of the errors.

The WFC3 instrument is most often used to search for signs of water in emission or transmission spectra due to a key water absorption feature at 1.4μm (Kirkpatrick, 2005). In order to test whether we could diagnose the presence or absence of water using a colour-magnitude diagram, we create a photometric band centred on the water feature between the *J* and *H* bands (W_{JH}-band hereafter) defined by integrating between 1.325 and 1.495μm. We therefore also add W_{JH}-band photometry for eleven planets to our database.

The inclusion of photometry in our newly created band meant that we also had to add host-star photometry in the same band. For this, we once again used Pickles standard spectra as described above.

2.3 Assembling a brown dwarf comparison sample

The beauty of a colour magnitude diagram is in how it enables simple comparison between population samples in a given wavelength space. A handful of objects on a colour-magnitude diagram by themselves do not allow us to infer much about these objects. Therefore, it is crucial that we have a large sample of well-studied objects to compare with our planets. As was done in Triaud et al. (2014), we make use of the detailed catalogue of near- and mid-infrared photometry of brown dwarfs produced by Dupuy & Liu (2012) to populate the background of our diagrams. Brown dwarfs are an excellent comparison sample as they overlap with exoplanets in temperature and radius, which leads to comparable luminosities (Triaud, 2014). For non standard bands,

and for photometric bands that we defined, such as W_{JH}, there are no brown dwarfs catalogs we could use. We therefore synthetically create brown dwarf magnitudes and colours by integrating their spectra, which helps us populate the diagram and provide a comparison sample.

The SpeX Prism Library[4] provides normalised near-infrared spectra of brown dwarfs spanning the wavelength range 0.8–2.5μm. These data are collected from the ground but are corrected for telluric absorption caused by water in the atmosphere (Rayner et al., 2003).

We initially downloaded 597 files available containing spectra for objects spanning the M to T spectral classes; we began by removing any duplicates. 2MASS *J*, *H* and *K* magnitudes were provided for the majority of them; we discarded any data where they were missing. We calculated apparent magnitudes using Vega as a reference once again, integrating the Kurucz spectrum in each band.

In order to test the validity of our method, we first combined the integrated Vega flux with the provided 2MASS magnitudes of each star to recover synthetic *J*, *H* and *K* magnitudes for the brown dwarfs. As each of the spectra are provided normalised, an important step in the determination of the magnitudes was to calculate a scale factor from each. These scale factors were determined by computing the band-integrated flux for each star in the same units as Vega's flux, working backwards with each of the 2MASS magnitudes:

$$F_{bd} = F_{vega} \times 10^{\frac{2MASS\,(mag)}{-2.5}} \qquad (2.2)$$

Where F_{bd} is the band-integrated brown dwarf flux in Vega's units, F_{vega} is Vega's band-integrated flux, and 2MASS (mag) is the 2MASS *J, H* or *K* magnitude of the brown dwarf. Dividing these fluxes by those obtained by integrating the spectra of the brown dwarfs yielded the required scale factors in all bands, which we then averaged. We used these to scale up the fluxes obtained by integrating the *J*, *H* and *K* fluxes. All fluxes were also scaled using the spectral response function of each of the photometric bands. Errors are propagated throughout. We present one-to-one plots of recovered *J*, *H* and *K* magnitudes in Figure 2.2, along with reduced χ^2. In these plots we can see that 2MASS *K* magnitudes are recovered with the greatest

---

[4]`http://svo2.cab.inta-csic.es/vocats/v2/spex/index.php`
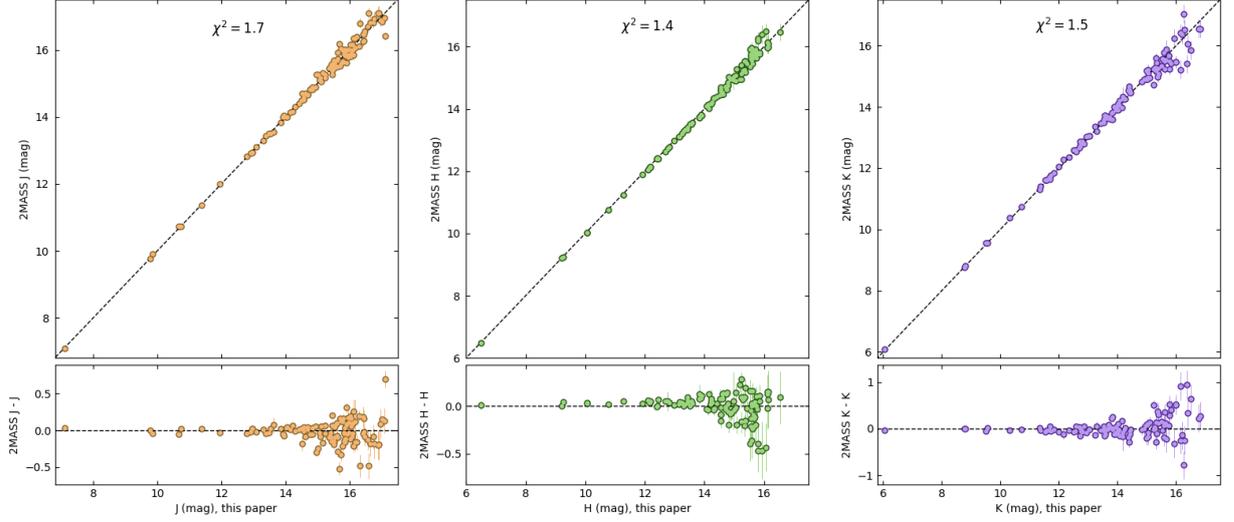
Figure 2.2: One-to-one plots of recovered *J*, *H* and *K* magnitudes for brown dwarfs compared with those provided in the literature. Residuals are presented in the lower panels and reduced χ^2 are given for each band.

uncertainties; plots of a random sample of SpeX spectra reveal that generally the noise is very large at longer wavelengths which leads to very low signal-to-noise ratio on these magnitudes.

This process resulted in a catalogue of photometry of 95 brown dwarfs. These were cross-referenced with the parallaxes provided by Dupuy & Liu (2012) in order to include distances in our catalogue.

2.4   Comparing with model atmospheres

It is also important to verify whether exoplanet atmospheric models match observations. We produce synthetic photometry from atmospheric model spectra. In this paper we chose to use the publicly available model spectra produced by Mollière et al. (2015) as they cover a wide parameter space, most importantly carbon-oxygen ratios of 0.35 to 1.40; effective temperatures of 1000K to 2500K in 250K increments; and five metallicity values, ranging from -0.5 to 2.0.

While we chose the Mollière models to demonstrate our code, it can adapted to use others as well. The data were processed using an adapted version of the code we used to produce magnitudes from SpeX data. One key difference between the SpeX and model spectra are that while each SpeX spectrum is provided normalised, the model spectra are in physical units: wavelengths are in cm and fluxes are in $mW \cdot m^{-2} \cdot Hz^{-1}$. As the Kuruzc spectrum is provided in

different physical units (wavelength in nm and flux in $\text{ergs} \cdot \text{cm}^{-2} \cdot \text{s}^{-1} \cdot \text{sr}^{-1} \cdot \text{nm}^{-1}$) a conversion factor had to be applied all data to achieve dimensional consistency.

The simplest solution adopted was to convert all wavelengths to μm and all fluxes to Janskys.

2.5   Blackbody Positions

In addition to comparing exoplanets with brown dwarfs, Triaud et al. (2015) showed how the positions of the planets compared with those of perfect blackbodies of comparable size and temperature. In order to reproduce this within our code, we make use of the Planck law to calculate the flux density as a function of wavelength and temperature (Planck & Masius, 1914):

$$B(\lambda, T) = \frac{2\,h\,c^2}{\lambda^5}\,\frac{1}{e^{\frac{h\,c}{\lambda k_B T}} - 1} \tag{2.3}$$

Where $B(\lambda, T)$ is the flux density of the blackbody, λ is the central wavelength of the photometric band, T is the temperature of the blackbody, and h, c and k_B are the Planck constant, the speed of light in a vacuum and the Boltzmann constant respectively. We calculated the flux density of Vega to use as a reference along with the blackbody fluxes.

In order to derive apparent magnitudes using Equation 2.1, we now convert the flux densities into flux ratios, using Vega as a reference:

$$F_{ratio} = \frac{F_{bb}}{F_{Vega}} \left(\frac{R_{bb}}{r_{bb}}\right)^2 \left(\frac{r_{Vega}}{R_{Vega}}\right)^2 \tag{2.4}$$

Where F_{bb} and F_{Vega} are the flux densities of the blackbody and Vega respectively, R_{bb} and R_{Vega} are the blackbody and Vega radii respectively, and r_{bb} and r_{Vega} are the distances to the blackbody and Vega respectively. In the case of r_{bb}, we set this value to 10pc so that our calculated magnitudes are absolute. In Figure 2.3 we present a small section of the code that demonstrates the implementation of Equations 2.3 and 2.4.

```
#Defines a function to calculate the spectral energy density at the central
# wavelength
def planck (T, band):
    fluxes = [(constant1/(band**5))*(1/(np.e**(constant2/(band*i))-1))
    for i in T ]
    return fluxes


def bbmags (band, radius, Tbb):
    fluxvega = planck (Tvega, band)
    fluxbb = planck(Tbb, band)
    flux_ratios = [(i/fluxvega[0])*((((radius*Rjupiter)/rbb)**2)/constant3)
    for i in fluxbb]
    mags = [-2.5*np.log10(i) for i in flux_ratios]
    mags = np.array(mags)
    return mags
```

Figure 2.3: Portion of `CMD.py` code showing the functions written to compute fluxes and magnitudes of blackbodies using the Planck function.

2.6 Description of our Python Toolkit

We have produced a selection of Python tools which automate all of the data analysis methods described above. Data handling is packaged into three modules: `Synth.py` to produce synthetic photometry of brown dwarfs from SpeX spectra; `Models.py` to produce synthetic photometry from model exoplanetary spectra; and `CMD.py`: a plotting module which computes planetary magnitudes and plots colour-magnitude diagrams. Below we give a brief outline of the modules and a walkthrough of the interactive Jupyter notebook.

2.6.1 `Synth.py`

This module provides a user with the flexibility to define bespoke photometric bands, in much the same way as we created our W_{JH}-band. New bands should be designed to coincide with interesting absorption features, which can be selected by inspection of brown dwarf spectra, or from line lists (e.g. Polyansky et al., 2018). Figure 2.4 shows model brown dwarf emission spectra (Baraffe et al., 2003; Allard et al., 2001) on which we have highlighted the 2MASS *J*, *H*, and *K* bands in lilac, along with *Spitzer*'s mid-infrared bands in shades of red. The hatched area corresponds to the section of the G141 grism we used, with the light blue hatched area indicating the position of our *W*-band. This plot shows how the 1.4μm water absorption widens and deepens with decreasing temperature.

It is important to bear in mind that a new band might not necessarily be useful for the full
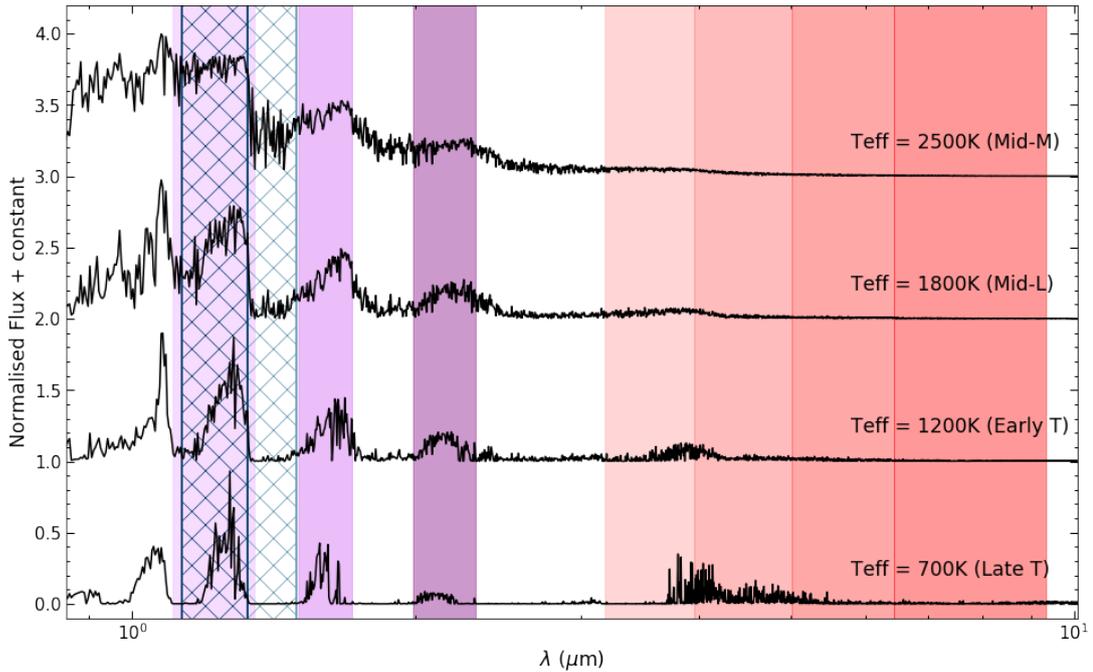
Figure 2.4: Model brown dwarf spectra, with photometric bands highlighted. In shades of red we have highlighted the position *Spitzer's* channels 1–4. The three bands in shades of lilac are 2MASS bands *J, H,* and *K*; the sections of the HST G141 grism we used are in blue hatching.

temperature range of brown dwarfs: the spectra of cooler objects is likely to be dominated by molecular species while hotter objects could have molecular, atomic or even ionised absorbers present. These changes are evident in the spectra shown in Figure 2.4, as well as the changing width of absorption features. Cooler objects are likely to need wider photometric bands to detect molecular features, whereas narrower bands are increasingly useful for the narrow absorption features seen in objects with higher temperatures.

Our `Synth.py` module contains seven built-in photometric bands, and all synthetic photometry will be produced in these bands along with a user-defined band. As well as the three 2MASS bands and our *W*-band, we have included HAWK-I's two narrow bands (NB1090 and NB2190) and Sloan's z'-band.

While this module has been written with SpeX spectra in mind specifically, it can easily be adapted to work with any other brown dwarf spectra. The function outputs either a text file or a spreadsheet with photometry in the desired bands, along with spectral types and astrometric distances.

18

2.6.2 `Models.py`

The `Models.py` module computes photometry from Mollière's model spectra. Although the code has been written with this particular set of models in mind, it can be used for any model spectra that are produced in physical units. The functions make use of the map provided by Mollière et al. (2015) to search for the spectrum which matches with the chosen parameters. The inputs required are constraints on metallicity, surface gravity, C/O ratio, effective temperature and host star spectral type. These constraints can be single values or lists of values; it is also possible to leave a parameter open which will result in all possible values being computed for that parameter. The two functions within the module output photometric magnitudes or colours respectively. There are eleven near- and mid-infrared bands built-in which can be called by name, and once again users can define bespoke bands if required.

2.6.3 `CMD.py`

This module reads the planet database we have assembled and computes colours and magnitudes of exoplanets. There are five plotting functions which use these data to produce colour-magnitude diagrams.

The first plotting function (`CMD_1`) produces diagrams in the style of those presented in Triaud et al. (2014). We have added a keyword argument to this and all other plotting functions (`adjusted`) which when called will adjust the absolute magnitudes of the exoplanets to a size of $0.9R_J$. This is to allow for a better comparison between planets, and to brown dwarfs. We chose this particular radius since typically brown dwarfs have a radius of $\approx 0.9R_J$ (Kirkpatrick, 2005) while Hot Jupiters are more diverse in size. This only corrects the measurement with a simple translation up or down in absolute magnitude.

The second and third plotting functions (`CMD_2` and `CMD_3`) both show a polynomial to represent the mean trend of brown dwarfs in order to clarify and de-clutter the diagrams; this is especially valuable in colours where we now have many planets plotted. The polynomials are positioned using coefficients computed by Dupuy & Liu (2012). The key difference between the second and third plotting functions is a keyword argument (`highlight`) present in `CMD_3` which

greys out all planets except those called by name. This allows objects of particular interest to be highlighted when needed.

The remaining two plotting functions make use of our new comparison samples. They call the functions from `Synth.py` and `Models.py` in order to compute the necessary photometry for the bands requested. When using the model plotting function (`CMD_model`), the model atmospheres can be coloured according to any of the five model parameters (C/O ratio, metallicity, surface gravity, effective temperature, or host star spectra type); in the synthetic brown dwarf function (`CMD_synth`) the ultra-cool dwarfs are coloured according to spectral type.

All plotting functions additionally include the ability to plot the position of a blackbody of comparable radius to the objects plotted on the diagram.

2.6.4 Tooklit Walkthrough

Users can interact with the CMD_toolkit via our Jupyter notebook applet, which makes use of HTML iPython Widgets[5]. This makes the experience far easier as plot options can be selected via drop-down boxes and tick-boxes rather than having to write lines of code. In this section we will show how the applet works and some of the available options.
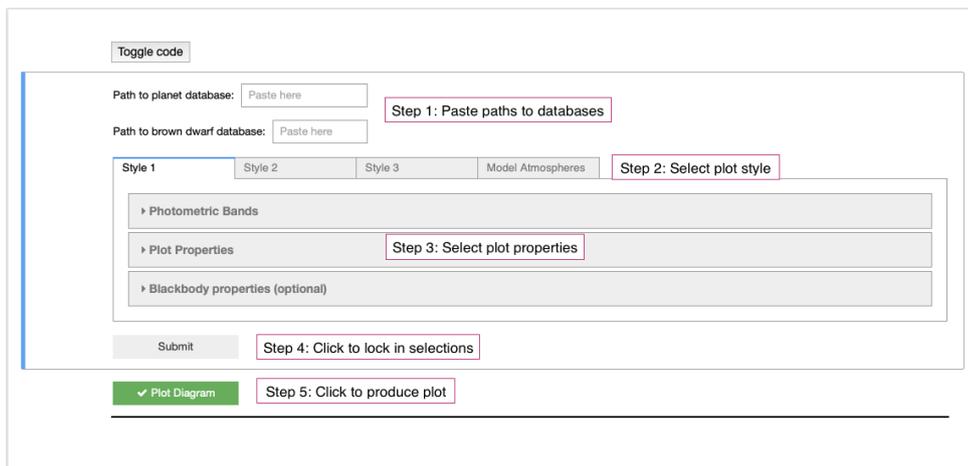
Figure 2.5: Applet view on first opening the Jupyter Notebook. Overlaid pink boxes show the order of steps to produce a colour-magnitude diagrams with our tools.

Figure 2.5 shows the applet as it appears on first opening the notebook. The code can be toggled on and off in order to see how the applet is interacting with the .py modules we have

---

[5]https://ipywidgets.readthedocs.io/en/stable/

Figure 2.6: Selecting planets to highlight on a colour-magnitude diagram. The names are not case-sensitive but there must be hyphens between letters and numbers. Planet letters are omitted in this version.

written. There are two boxes where users can paste the paths to the planet and brown dwarf databases after downloading them from Github. Once all selections for a particular style of plot have been made, the 'Submit' button must be clicked in order to lock in all settings. The 'Plot Diagram' button will then call the correct plotting function with all necessary key word, and the plot will appear below the applet.

The 'Style 1' tab corresponds to the function CMD_1, which produces colour-magnitude diagrams in the style of those presented in Triaud et al. (2014). 'Style 2' calls the function CMD_2 and outputs plots in the same style as Figure 3.6. For the function CMD_3, which allows users to highlight specific planets in a different colour as in Figures 3.3 and 3.4, users should select the 'Style 3' tab. Here it is necessary to enter the name of the host star placing a hyphen between letters and numbers. See Figure 2.6 for an example.

The tab labelled 'Model Atmospheres' allows users to create colour-magnitude diagrams using the function CMD_model in order to compare synthetic photometry with real planets. There are many options to choose from when setting the model spectra. Some defaults are always selected as constraining nothing will lead to photometry being computed for all 10,640 available spectra. While this can be done, it will be time consuming so users should only select 'all' for each parameter if that is what they wish to do. Figure 2.7 shows the layout of the accordion for this style of diagram.

All four styles of plot have the same photometric bands available and can have a 0.9R$_J$
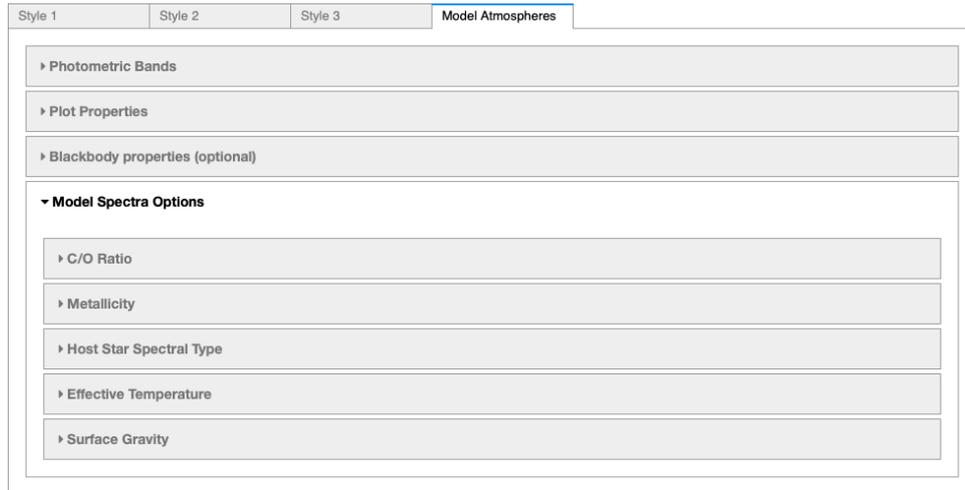
Figure 2.7: 'Style 3' and 'Model Atmospheres' both have an extra element compared with 'Style 1' and 'Style 2'. Here we show the view for 'Model Atmospheres' with a closed accordion.

blackbody added to the diagram. They can also have a colourbar included or not, and can have planetary magnitudes adjusted to the size of a $0.9R_J$ object.

3 RESULTS

Section 3.2 was written specifically for this paper, while the remaining sections are verbatim reproductions from a paper in preparation on which I will be first author.

We begin this chapter with a brief explanation of how to read a colour-magnitude diagram, along with some of the terminology to expect.

In Section 3.2 we present updated versions of all the colour-magnitude diagrams first presented in Triaud et al. (2014), accompanied by descriptions of their key features. We then go into further detail with a selection of plots to illustrate how powerful it can be to view results for individual planets in context.

In Section 3.3, we show how a colour-magnitude diagram can allow us to select stand-out objects for rapid follow-up, and Section 3.4 outlines how inconsistency between colours of planets and brown dwarfs led us to investigate the absence of Phosphine in irradiated objects. In Section 3.5 we demonstrate how a colour-magnitude diagram can be used to get a quick constraint on the C/O ratio.

3.1 Notes on Terminology

The x-axis of a colour-magnitude diagram is a colour index, calculated as the difference in magnitude between two photometric bands. It is conventional to subtract a longer wavelength magnitude from a shorter wavelength magnitude; this convention is observed throughout our paper.

In a conventional colour-magnitude diagram objects can therefore be compared in terms of their x-position on the plot: an object on the left hand side would be described as 'bluer' than one on the right hand side. This is due it having more flux, and therefore a higher magnitude,

in the shorter, bluer wavelength than in the longer, redder wavelength. The converse is true of 'redder' objects. When describing the spread of objects on our colour-magnitude diagrams, we will therefore use the terms 'bluer' and 'redder' to refer to placements on the left and right hand sides respectively.

3.2 Updated colour-magnitude diagrams

In this section we present updated versions of all colour-magnitude diagrams first presented in Triaud et al. (2014). These are plotted implementing our new Python toolkit.

3.2.1 Near-infrared colour-magnitude diagrams

In Figure 3.1 we present updated colour-magnitude diagrams in the *2MASS* photometric bands, *J*, *H* and *K*. The absolute magnitudes of planets have been scaled to a $0.9R_J$ object coincide with the typical size of a brown dwarf. Additionally, we have plotted the location of a $0.9R_J$ blackbody at temperatures of 1500K, 2500K, 3500K and 4500K. The mean position of the brown dwarf sequence is shown by a polynomial coloured by spectral type, computed using coefficients provided by Dupuy & Liu (2012). Due to the low number of *J*-band fluxes measured for exoplanets, we have supplemented the data with our photometry computed from HST/WFC3 low resolution spectra.

The small number of planets presented in Triaud et al. (2014) appeared to be equally compatible with the ultra-cool dwarfs and the blackbody sequence. This remains the case, which is in agreements also with the near-infrared colour-magnitude diagrams presented recently in Manjavacas et al. (2019). Parmentier et al. (2018) writes that objects belonging to the subclass of ultra-hot Jupiters should lack any emission and absorption features, instead resembling a blackbody. At this time is is still impossible to disentangle which family of objects the planets resemble most; all objects which appear excessively blue or red have errors which make interpretations ambiguous. However, in Section 3.5 we see that in our newly created mid-infrared, the W_{JH}-band, we begin to see a departure from both the blackbody sequence and the narrow spread in colour of the M and L brown dwarfs.
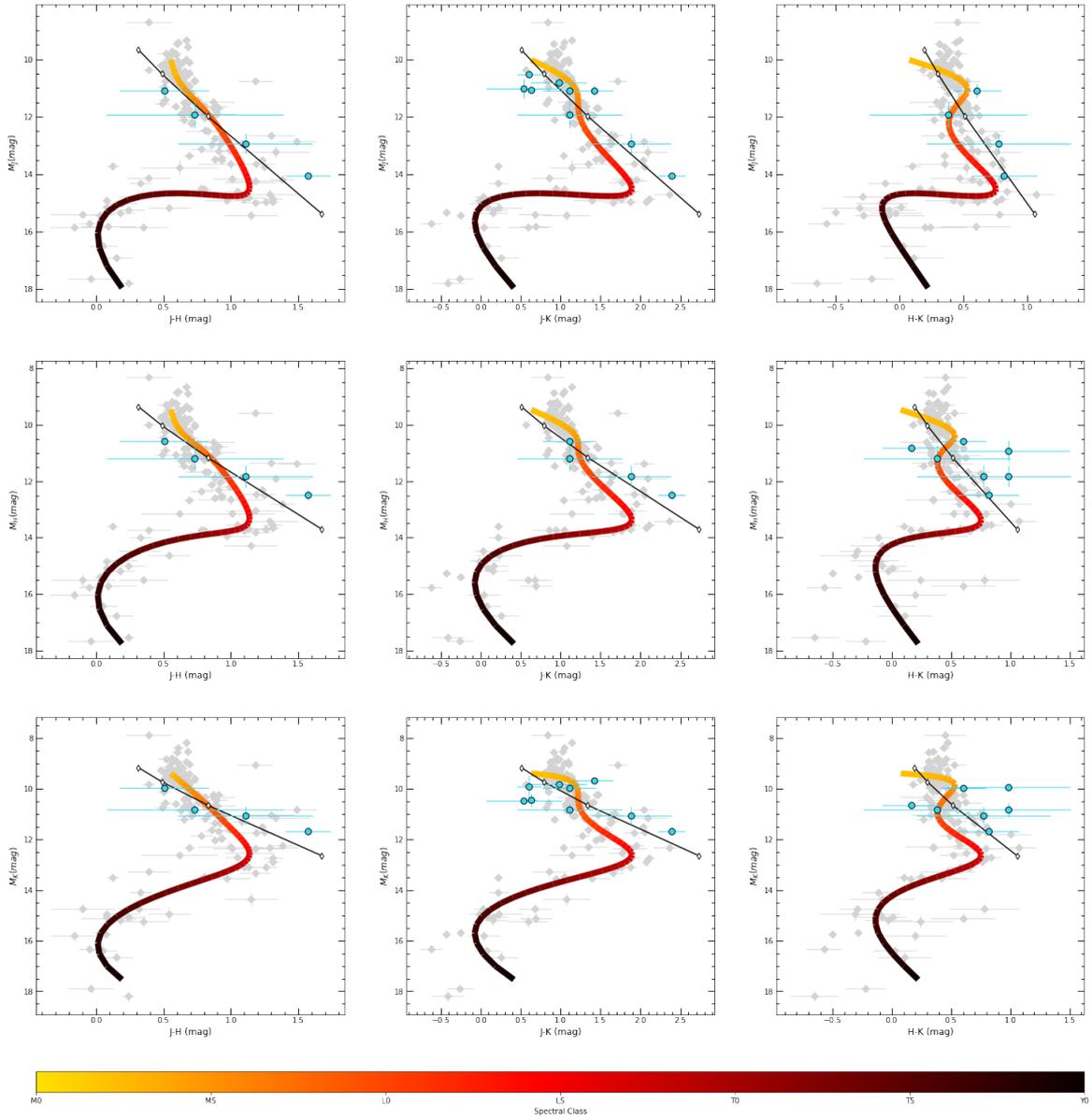
Figure 3.1: Updated near-infrared colour-magnitude diagrams in near-infrared photometric bands, similar to those first published in Triaud et al. (2014), plotted using our `CMD_2` plotting function. Magnitudes have been adjusted to coincide with an object of radius $0.9R_J$ for easier comparison with brown dwarfs. We have also plotted in black the location of a $0.9R_J$ blackbody as a black line; the white-filled diamonds show the position of the blackbody at temperatures of 1500K, 2500K, 3500K and 4500K. The polynomial representing the mean sequence of the brown dwarfs has been coloured according to spectral type.

3.2.2 Mid-infrared colour-magnitude diagrams

In Figure 3.2 we present updated colour-magnitudes in *Spitzer's* mid-infrared channels 1-4. Absolute magnitudes have once again been scaled to facilitate comparison with brown dwarfs. In black we show the blackbody sequence, with the unfilled diamonds indicating the position of a $0.9R_J$ blackbody of temperature 750K, 1750K, 2750K, 3750K and 4750K. We continue to plot the mean sequence of brown dwarfs using polynomial coefficients as above.

The biggest increase in measurements can be seen in the top two plots on the far left, principally due to the contribution from Garhart et al. (2019). There is some increased scatter evident in these plots, and in $M_{4.5}$ vs [3.6μm - 4.5μm] in particular we are beginning to see an emerging sub-population of cooler objects which depart from both the brown dwarfs and the blackbodies. We explore this further in Section 3.3.

3.3 Outliers and Emerging Sub-populations

In this subsection, we go through a few examples on how colour-magnitude diagrams can be used to select target for additional observations, asking questions about patterns in the data, and diagnosing molecular signatures.

3.3.1 Identifying oddball systems and measurements

Figure 3.3 is a colour magnitude diagram made with our plotting function `CMD_3`. As we are comparing planets and brown dwarfs we have used the key word argument `adjusted` to scale the magnitudes to the size of a typical brown dwarf. On this plot we have highlighted two objects which are clear outliers, and one which is not.

On the top left we have HAT-P-2b, a highly eccentric planet (e $\approx$ 0.5 (Lewis et al., 2013)) that is speculated to have a dayside temperature inversion. In [3.6μm - 4.5μm] it is consistent with both the L-Dwarf sequence and the mean position of other planets, which indicates that the 5.8μm flux is the one causing its very blue colour. The surprisingly shallow secondary eclipse in *Spitzer*'s Channel 3 was noted at the time of measuring, as it yields a brightness temperature ~700K lower than the secondary eclipses measured in Channels 1, 2 and 4. If this low flux in
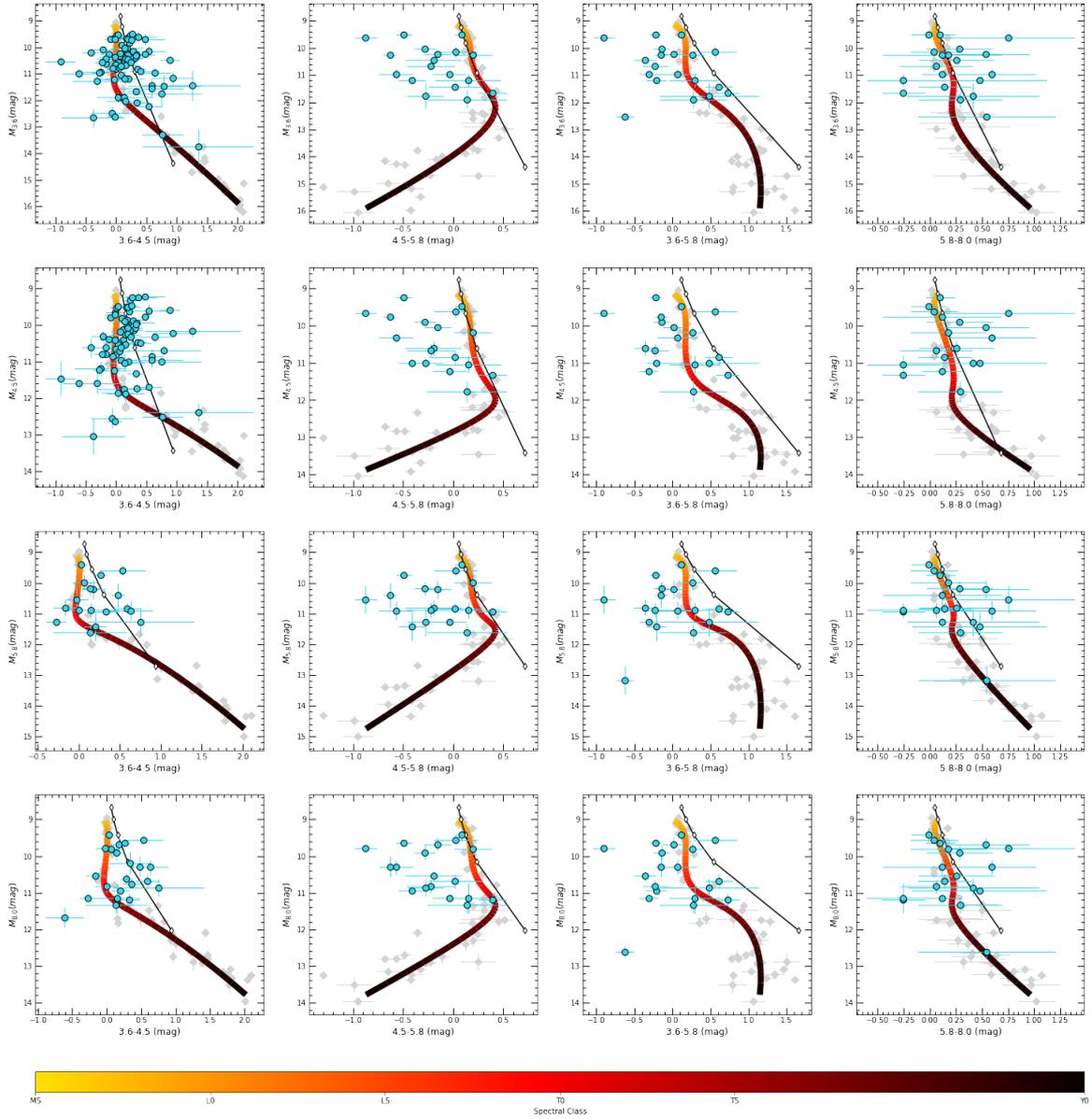
Figure 3.2: Updated near-infrared colour-magnitude diagrams in mid-infrared photometric bands, similar to those first published in Triaud et al. (2014), plotted using our `CMD_2` plotting function. Magnitudes have been adjusted to coincide with an object of radius $0.9R_J$ for more straight-forward comparison with the brown dwarf sequence. As before, we have also plotted a $0.9R_J$ blackbody with a black line, highlighting temperatures of 750K, 1750K, 2750K, 3750K and 4750K. The polynomial representing the mean sequence of the brown dwarfs has been coloured according to spectral type.
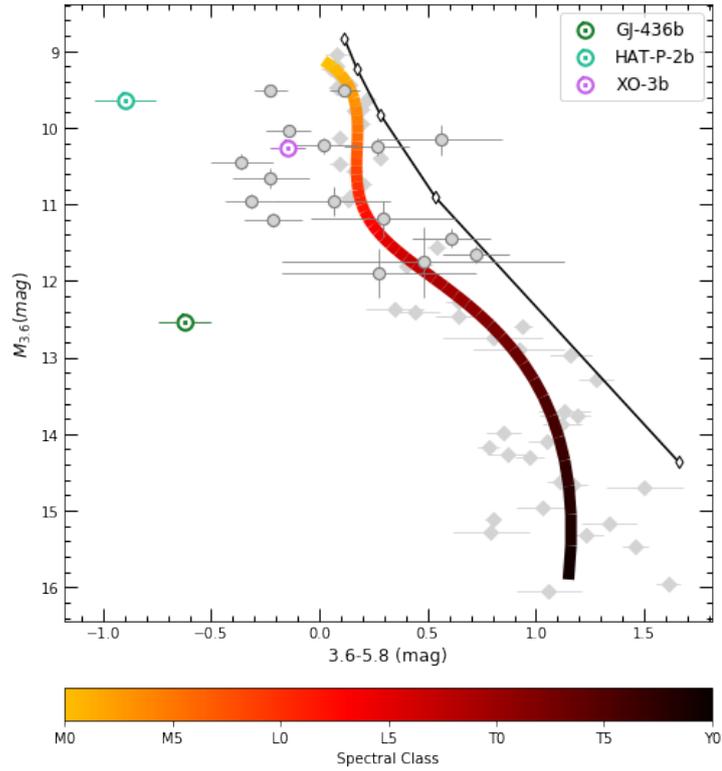
Figure 3.3: Colour-magnitude diagram in $M_{3.6}$ vs. [3.6μm - 5.8μm] using our function `CMD_3`. Planetary magnitudes have been scaled to a 0.9R$_J$ object for better comparison with the brown dwarfs. The black line shows the position of a 0.9R$_J$ blackbody with the white-filled diamonds showing the position of the blackbody at temperatures of 750K, 1750K, 2750K, 3750K and 4750K. The polynomial showing the mean position of the brown dwarfs sequence is once again coloured according to spectral type.

the 5.8μm band is caused by processes unique to eccentric hot Jupiters, then it is possible that further eccentric systems will be similarly blue in this colour.

Further down on the same plot, we have GJ 436b. This object is also eccentric (e $\approx$ 0.14 (Maciejewski et al., 2014b)) yet in this case the problematic flux is in the 3.6μm band. This is confirmed by its position on a $M_{5.8}$ vs [5.8μm - 8.0μm] where it intersects exactly with the brown dwarf sequence.

GJ 436b is a warm Neptune with an equilibrium temperature of $\approx$700K (Turner et al., 2016), while HAT-P-2b is a hot Jupiter with an equilibrium temperature of 1540K (Pál et al., 2010). Following up on both of these objects will allow us to determine whether their blue colours in [3.6μm - 5.8μm] are in any way caused by their eccentricity, and if so it could point to key population differences between Jupiter and Neptune-sized objects.

We have highlighted one other planet on Figure 3.3: XO-3b is the only other planet with

a significant eccentricity (e significant > 0.1) on this plot (e ≈ 0.28 (Machalek et al., 2010)). The 3.6μm and 5.8μm fluxes for XO-3b have not been updated since 2010, and the values come from single eclipse measurements. When the 4.5μm flux was remeasured in 2014 by Wong et al. (2014) they calculated a deeper eclipse of 0.158% which differs by 2.1σ from the original. This new eclipse depth was derived from 12 consecutive secondary eclipse events, and the mean variation between them of just 5% indicates no consequential orbit-to-orbit variation.

Both of the HAT-P-2b fluxes were also calculated from single secondary eclipse events. For GJ 436b, the 3.6μm flux has been remeasured since the first observations of its thermal emission, but the 5.8μm has not; this latter value also came from a single eclipse event. Hansen et al. (2014) has claimed that these flux ratios measured from single events have low reproducibility and underestimated errors as they do not adequately account for instrument systematics. This throws into question the significance of results inferred from single-eclipse photometry.

A further stand-out system can be seen in Figure 3.4: on the far left with a colour of -0.9 we find WASP-65b. WASP-65b is one of the densest known hot Jupiters in its mass regime (R = 1.112R_J, M = 1.55M_J); it orbits in an area where inflated radii are the norm (a = 0.0334AU) yet it is denser than Jupiter itself (Gómez Maqueo Chew et al., 2013). It has been suggested that its uninflated radius could be evidence of the advanced age of the system, and that if this is the case, the contraction of its atmosphere could lead to changes in its temperature-pressure profile giving rise to unexpected spectral features. The measurements for WASP-65b also result from observations of a single eclipse event (Garhart et al., 2019).

These four planets are clear candidates for follow-up. The data so far is indicative that eccentricity and density might cause an important difference in atmospheric properties in two cases. It is however more likely that a lack of repeated measurement is the root cause. Regardless of what the answer turns out to be, using a colour-magnitude diagram simplifies the process of target selection.
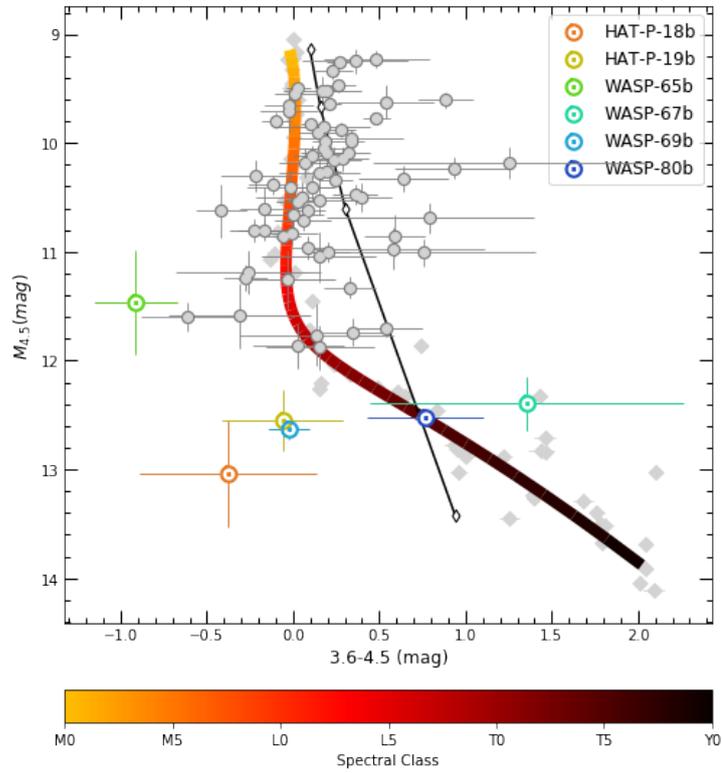
Figure 3.4: Colour-magnitude diagram in $M_{4.5}$ vs. [3.6μm - 4.5μm] using our function `CMD_3`. Planetary magnitudes have been scaled to a 0.9R$_J$ object for better comparison with the brown dwarfs. The black line shows the position of a 0.9R$_J$ blackbody with the white-filled diamonds showing the position of the blackbody at temperatures of 750K, 1750K, 2750K, 3750K and 4750K. As before, the polynomial showing the mean position of the brown dwarfs sequence is coloured according to spectral type.

3.3.2 Planets near the T spectral class

In Figure 3.4 we present a colour-magnitude diagram in $M_{3.6}$ vs. $[3.6\mu m$ - $4.5\mu m]$. The five planets we have highlighted all have equilibrium temperatures of between 800-1000K, with HAT-P-18b and WASP-80b being the coolest of the set. Triaud et al. (2015) pointed out that WASP-80b was the first planet whose measured dayside flux fell in a position consistent with the L-T transition experienced by ultra-cool dwarfs between 1100-1500K. This transition is characterised by the emerging spectral signature of methane, which has its fundamental band at $3.3\mu m$ and is therefore detectable by *Spitzer*'s Channel 1. Triaud et al. (2015) suggested that this could be indicative that planets undergo a similar transition but at a lower temperature. The fact that we now have fluxes measured for HAT-P-18b which is comparable in temperature and radius (Wallack et al., 2019), yet is significantly bluer, indicates that perhaps this is not true of all cool exoplanets.

One way in which these two planets differ is in mass: WASP-80b is approximately three times more massive than HAT-P-18b ($0.55M_J$ vs. $0.183M_J$). Additionally, we find that WASP-67b, whose colour is also consistent with that of an early T-dwarf, is more than twice as massive as HAT-P-18b (Kammer et al., 2015). HAT-P-19b ($0.292M_J$) and WASP-69b ($0.25M_J$) fall between the others in both colour and mass. This is still too small a sample for a proper inference, however so far, there is an interesting indication in the transition from L to T class (CO to CH_4 chemistry) that increased mass might be correlated with a redder colour in $[3.6\mu m$ $-4.5\mu m]$.

This ties in well with the conclusions of Zahnle & Marley (2014), who showed that the temperature of transition from CO-dominated to CH_4-dominated atmospheres scales with gravity. As the densest of the five, WASP-80b also has the highest surface gravity which would point to a higher temperature to undergo the planetary version of an L-T transition. We summarise the masses and radii of these five planets in Table 3.1.

An alternative interpretation for the range of colour that these planets cover might arise as differences in metallicity and C/O ratio. Kammer et al. (2015) sought to find a link between mass, metallicity and C/O ratio for cool exoplanets, with HAT-P-19b and WASP-67b included

Planet	Mass (M_J)	Radius (R_J)	Ref.
HAT-P-18b	0.200±0.019	0.995±0.052	253
HAT-P-19b	0.292±0.018	1.132±0.072	102
WASP-67b	0.43±0.09	1.15±0.11	229
WASP-69b	0.250±0.023	1.057±0.047	253
WASP-80b	$0.538^{+0.035}_{-0.036}$	$0.999^{+0.03}_{-0.031}$	247

Table 3.1: Masses and radii of five of the planets highlighted on Figure 3.4.

in their sample. They found a tentative link between the masses of cool planets and the ratio of $3.6\mu m$ and $4.5\mu m$ magnitudes, which is consistent with the suggestion that less massive planets have higher metallicities (Moses et al., 2013b). More recently, Wallack et al. (2019) found that for cool planets, extreme values of C/O ratio lead to big shifts in atmospheric chemistry, having large effects on the [$3.6\mu m$ - $4.5\mu m$] colour. Our synthetic photometry of model atmospheres shows a very similar trend.

Figure 3.5 shows a colour-magnitude diagram created using `CMD_model()`. The Mollière spectra chosen correspond to a planet with T_{eff} = 1000K, log g = 3.0 and host star spectral type = G5. We found that this colour was not sensitive to host star spectral type, but showed some changes for values of log g $\geq$ 4. We can see that in this temperature regime, objects with a metallicity 0 experience a dramatic shift in colour with very small changes in oxygen abundance (between C/O = 0.7 and C/O = 0.85).

This shows that in principle, we could diagnose limits on both C/O ratio and metallicity for exoplanets under 1000K simply by measuring thermal emission in these two bands, and without extensive retrieval methods. For example the only objects with colours of 0.25 or lower are oxygen-rich ones. We also see that the very bluest colours only occur with a combination of oxygen-richness and high metallicity. Colours close to 1 indicate both high metallicity and a C/O $\geq$ 0.85.

At the time of writing this relationship is not yet calibrated. In Section 4.3 we outline the problem of model spectra which are not fully calibrated to real data. To account for this, the colours in Figure 3.5 have been offset by -1 magnitude. This offset is an approximation from inspection of the mean offsets in $M_{3.6}$ and $M_{4.5}$ as can be seen in Figure 4.2.
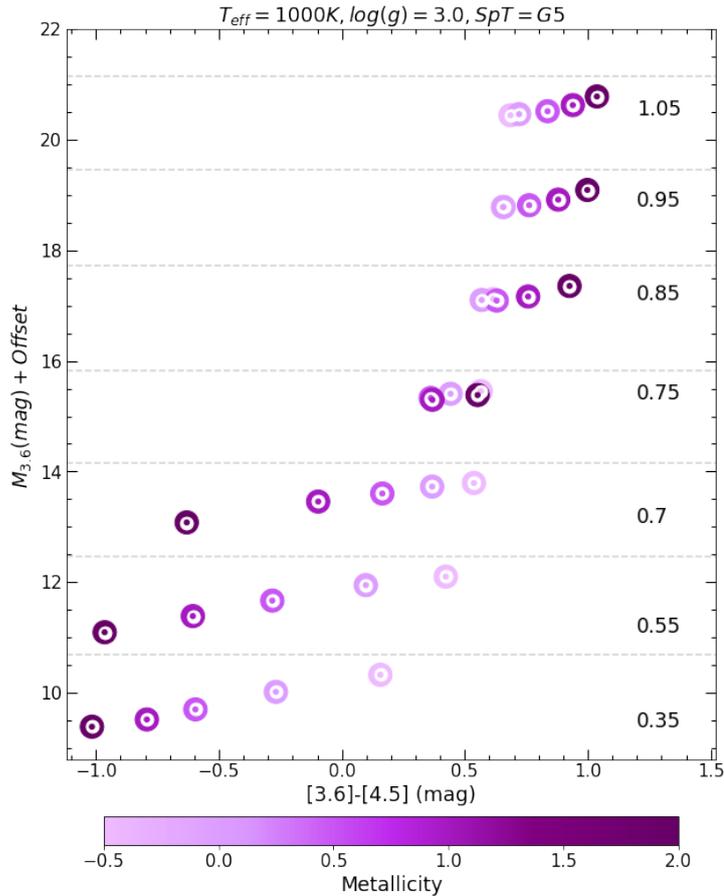
Figure 3.5: Colour-magnitude diagram of $M_{4.5}$ (plus an arbitrary offset) vs [3.6μm - 4.5μm] using model spectra. The colours have been offset by -1 magnitudes (see Section 4.3 for an explanation of the motivation). Points are coloured according to their assigned metallicity and each row of points represents model spectral with a different C/O ratio, as detailed on the right-hand-side of each row.

3.4   Identifying molecular Signatures

One interesting prospect for colour-magnitude diagram would be their ability to diagnose the presence of certain molecules, which would help setting up certain retrieval schemes.

A plot similar to Figure 3.6 appeared in Triaud et al. (2014). who highlighted a large discrepancy between the colours of brown dwarfs and hot Jupiters. Even with our improved distance measurements and absolute magnitudes adjusted to 0.9R$_J$, we can clearly see that planets are systematically bluer than brown dwarfs. This is in contrast with most near- and mid-infrared colour-magnitude diagrams where the planets are largely consistent in both colour and magnitude with the L-dwarf sequence (see Appendix 3.2 for up-to-date colour-magnitude diagrams). In Triaud et al. (2014) we suggested that the discrepancy in [4.5μm - 5.8μm] could
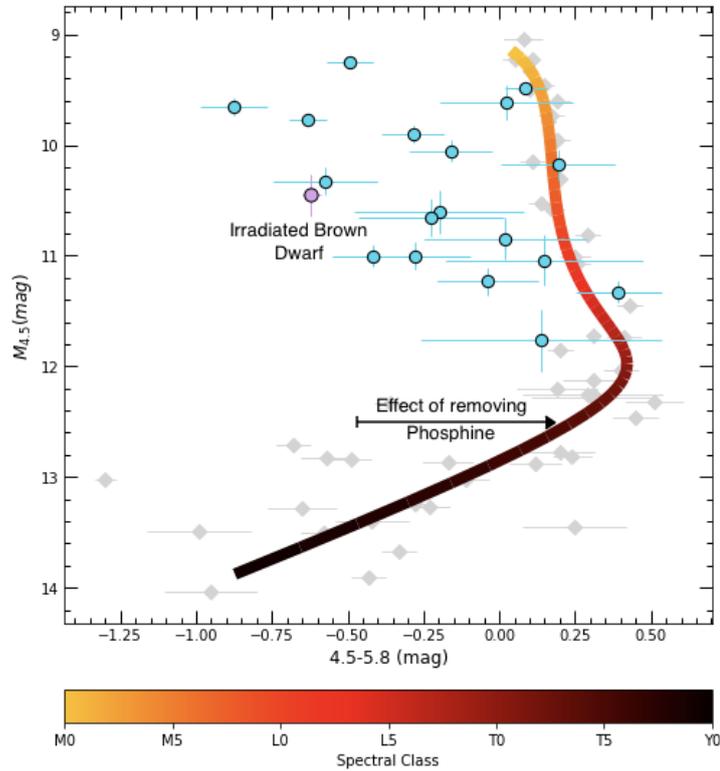
Figure 3.6: Colour-magnitude diagram showing the comparative blueness of planets with respect to brown dwarfs of similar brightness. The planetary absolute magnitudes have been scaled to a size of $0.9R_J$ for better comparison with brown dwarfs. We have highlighted in lilac the position of the irradiated brown dwarf WD0137-349B. The black arrow indicates the effect on this colour of removing phosphine.

perhaps be explained by an additional absorber within the $4.5\mu m$ band, present for the brown dwarfs but not for the exoplanets. We reached this conclusion because $5.8\mu m$ measurements of exoplanets appear consistent with brown dwarfs'.

An important difference between brown dwarfs and hot Jupiters is that while brown dwarfs are self-luminous, hot Jupiters are irradiated objects. We searched the literature to find out what irradiation could produce in relation to the $4.5~\mu m$ band. We identified Phosphine, PH_3, as a molecule present within brown dwarf atmospheres, but most likely absent in hot Jupiters (due to photolysis), as the cause of the discrepancy.

Phosphine has a strong absorption feature at approximately $4.3\mu m$ (Sharp & Burrows, 2007) and is identified as the most likely Phosphorus-carrying gas in the atmosphere of hot T-dwarfs and cool L-dwarfs, with temperatures in the range 1000K - 1400K (Visscher et al., 2006). However, PH_3 is highly susceptible to irradiation (Sousa-Silva et al., 2019), and expected to be

photodissociated in the upper atmospheres of hot Jupiters and other highly irradiated objects.

We sought to verify our hypothesis by searching for an irradiated brown dwarf with an eclipse measurement in the bands that we considered. There is only one such object to our knowledge, WD0137-349B (Casewell et al., 2015). This object is part of a white dwarf - brown dwarf binary and as such its dayside is subject to high levels of irradiation. We plot WD0137-349B's irradiated side on Figure 3.6 (Casewell et al., 2015). Its position on the colour-magnitude diagram is more consistent with the most irradiated exoplanets rather than the ultra-cool dwarfs. We interpret this as indication that irradiation is likely the cause of a higher than usual flux in the 4.5 μm channel. Since Phosphine does absorb in that particular band, and is expected to be within brown dwarfs' atmospheres, but not within hot Jupiter, we deduce that a lack of Phosphine may provide a good explanation for the 4.5 μm measurements.

To further investigate whether Phosphine can have the effect we thought, we used a model spectrum of GJ 504b produced with and without PH_3 present (Baudino et al., 2017). We integrated this spectra and found that the removal of PH_3 from the atmosphere causes a reddening of 0.65 *mag* in [4.5μm - 5.8μm]. We have added an arrow of this size to Figure 3.6 to illustrate the impact of PH_3 in this colour, which has an amplitude consistent with the difference between brown dwarfs and hot Jupiters, and between the irradiated brow dwarf WD0137-349B and its field brethren.

One further interesting feature of Figure 3.6 is that the amplitude of the colour offset between brown dwarfs and hot Jupiters increases with decreasing absolute magnitude (i.e. increasing equilibrium temperature). Equilibrium temperature is obviously related with insolation. If the bluer colours of planets are caused by the photodissociation of PH_3, then higher levels of insolation would be expected to lead to higher PH_3 depletion.

Could it be something else? Madhusudhan & Seager (2011) describe how *Spitzer* fluxes, and therefore our colours, can be interpreted based on knowledge of the location of spectral features of the key absorbers present in an atmosphere. Most notably, they state that these interpretations are based on the assumption that H_2O, CH_4, CO and CO_2 are the four dominant molecules in all *Spitzer* bands. Of these four, CO and CO_2 both have strong absorption features in the 4.5μm

channel, so low fluxes in this band are usually attributed to one or both of these molecules. However, thermal equilibrium predicts that both brown dwarfs and hot Jupiters should have most of their atmospheric carbon locked into CO in this temperature regime. We therefore return to our 'additional absorber' hypothesis.

An alternative explanation is to invoke thermal inversions in the vast majority of the hot Jupiters depicted in Figure 3.6. With such an inversion, CO would be in emission and increase the flux in the $4.5\mu m$ band. However, as we discuss 4.2, evidence for thermal inversion is scarce, and their existence is doubted by several authors.

3.5 Seeking to constrain the C/O ratio with colour-magnitude diagrams

In Figure 3.7 we present a colour-magnitude diagram featuring our new W_{JH} band, made with our `CMD_synth()` function; from brightest, the three planets plotted are WASP-12b, HAT-P-32Ab, WASP-43b. We computed the brown dwarf photometry with our `Synth.py` code, and we computed photometry for the three planets by integrating low resolution emission spectra measured with the Hubble Space Telescope's WFC3 G141 grism.

We have yet to identify a colour where objects with confirmed water detections are easily distinguishable from those without, however we can see that three objects in 3.7 are widely spread in colour which we will attempt to explain in this section. Incidentally, all three of these planets have firm detections of water using these data.

The H-band is centered on 1.6μm and has a prominent CH_4 absorption feature, and a slightly weaker CO feature (Sharp & Burrows, 2007), while the W_{JH}-band is dominated by water absorption. These four molecules are related by the following net equilibrium equation, as described in Madhusudhan (2012):

$$CH_4 + H_2O \underset{T \lesssim 1000K}{\overset{T \gtrsim 1000K}{\rightleftharpoons}} CO + 3H_2 \tag{3.1}$$
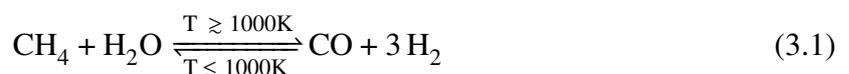
In objects cooler than 1000K the left hand side of the equation is favoured and methane is
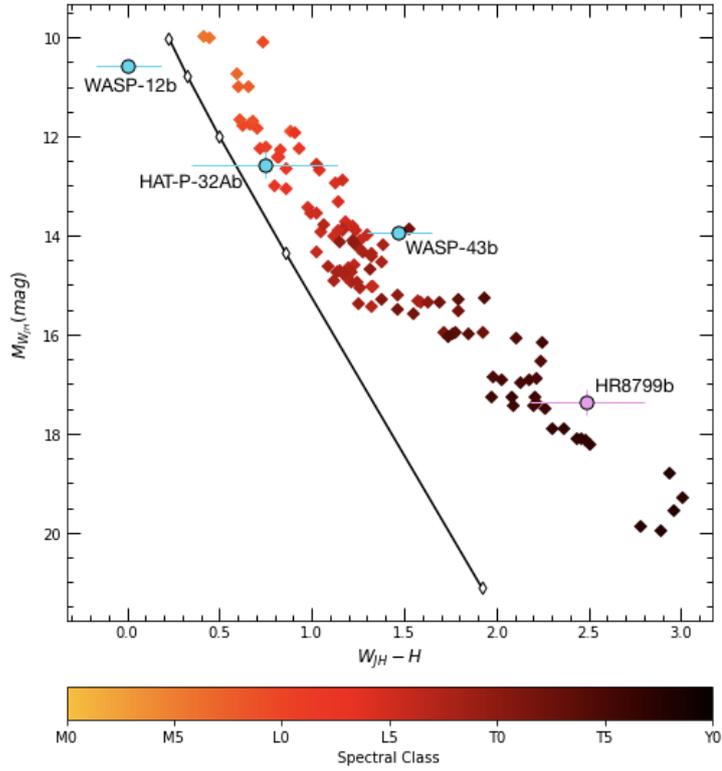
Figure 3.7: Colour-magnitude diagram of $M_{W_{JH}}$ vs. $[W_{JH} - H]$ usinf our plotting function `CMD_synth`. Planetary magnitudes have been scaled to a $0.9R_J$ sized object to allow better comparison with the brown dwarfs. The black line shows the position of a $0.9R_J$ blackbody, with the white-filled diamonds highlighting the position at temperatures of 1000-5000K in steps of 1000K. HR8799b is highlighted in lilac as its photometry was taken with direct imaging rather than secondary eclipse observations (Rajan et al., 2015; Marois et al., 2008).

the dominant carbon-bearing molecule. For objects hotter than 1000K, carbon is found mainly in the form of carbon monoxide. However, if a hotter atmosphere is also oxygen rich, we would expect the excess oxygen to react with the H_2 to form water. This indicates that C/O ratio should be the biggest indicator of both $[W_{JH}\text{-}H]$ colour and water abundance: more excess oxygen will cause more water to be produced. This will deepen the absorption at 1.4μm leading to increased W_{JH} magnitude, and therefore a redder colour. This is consistent with the retrieved water abundances for WASP-12b and WASP-43b by Line et al. (2014): WASP-43b's abundance was found to be greater than WASP-12b's by a factor of 10^3.

Figures 3.8 and 3.9 colour-magnitude diagrams featuring Mollière model atmospheres. Both have been plotted for four values of log g from 2.3 to 5.0, seven values of effective temperature from 1000–2500K, and a host star spectral type of G5. Figure 3.8 features atmospheres with a
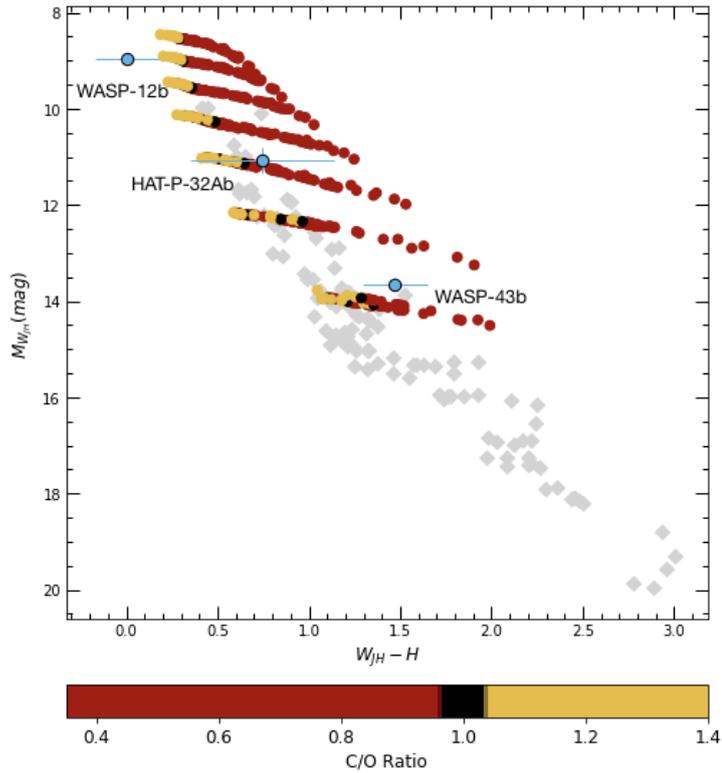
Figure 3.8: Colour-magnitude diagram of $M_{W_{JH}}$ vs. $[W_{JH} - H]$, plotted using our function `CMD_model`. The following parameters were entered for the model: T_{eff} = 1000 – 2500K, log g = 2.3, 3.0, 4.0 and 5.0, SpT = G5, and [Fe/H] = -0.5. Points have been coloured according to C/O ratio in order to highlight the differences between carbon- and oxygen-rich atmospheres.

metallicity of -0.5, while in Figure 3.9 we have assigned a metallicity of 2.0. The models have been coloured according to their C/O ratio.

We can see from Figure 3.8 just how much $[W_{JH}\text{-}H]$ colour is affected by the C/O ratio, and for two of the planets here plotted we can attempt to infer whether they are consistent with oxygen- or carbon-rich model spectra.

Withing its uncertainties, WASP-43b colours and magnitudes are consistent with an oxygen-rich atmosphere for all values of surface gravity, and retrievals of its metallicity have found it to be 0.3–1.7 × Solar (Kreidberg et al. (2014), Stevenson et al. (2017)). Therefore it is best matched by Figure 3.9, and we can see that its colour is indicative of an oxygen-rich atmosphere. This is in agreement with the upper limit set by Benneke (2015), and indeed with the recent retrieval by Irwin et al. (2019).

In contrast, WASP-12b's eclipse measurements coincide with the carbon-rich model atmo-
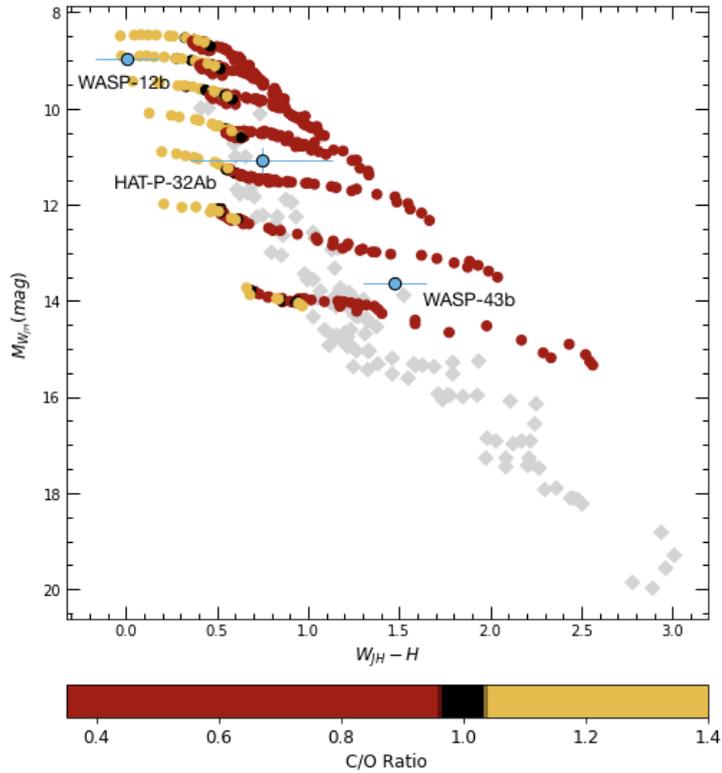
Figure 3.9: Colour-magnitude diagram of $M_{W_{JH}}$ vs. $[W_{JH} - H]$, plotted using our function `CMD_model`. The following parameters were entered for the model: $T_{\text{eff}} = 1000 - 2500K$, log g = 2.3, 3.0, 4.0 and 5.0, SpT = G5, and [Fe/H] = 2. As before, points have been coloured according to C/O ratio in order to highlight the differences between carbon- and oxygen-rich atmospheres.

spheres for both extremes of metallicity and all values of surface gravity. This is in agreement with Madhusudhan et al. (2011a) who found C/O ≥ 1 using *Spitzer* secondary eclipse data. This has since been contested, with Kreidberg et al. (2015) finding that the atmosphere was best fit by C/O ≈ 0.5 using HST transit data, but omitting *Spitzer* transits due to instrument systematics. Benneke (2015) also retrieved an oxygen-rich atmosphere with C/O < 0.9 for WASP-12b, even though analysis of previously unpublished *Spitzer* measurements by Stevenson et al. (2014b) had confirmed the original findings. We need a better understanding of the physical processes that lead to WASP-12b appearing consistent with carbon-rich model atmospheres; additionally, in order to confirm this consistency we need to ensure that the models are well calibrated to the data in this colour. This is discussed in more detail in Chapter 4.

We were unable to find a constraint on HAT-P-32Ab's C/O ratio in the literature, and due to the large errors on the colour we find that it is equally compatible with carbon-rich and

oxygen-rich model atmospheres.

4 DISCUSSION

This chapter is lifted verbatim from the section of the same name in a paper currently in preparation on which I will be first author.

In the following sections we discuss the implications of our results, placing them in the context of unexplained low fluxes and exciting upcoming missions.

4.1 Phosphine in exoplanetary atmospheres

The recently updated line list for phosphine published by Sousa-Silva et al. (2015) puts us in a favourable position to identify planets where this gas may be present. Over the lifetime of *Spitzer* there have been many unexplained low fluxes measured in Channel 2. In this section we speculate about the impact that Phosphine may have for a number of eclipse measurements, and planetary environments.

The absence of PH_3 on the daysides of hot Jupiters due to high levels of irradiation would not preclude the possibility of its presence on the cooler and less irradiated nightsides. One such candidate is HD 189733b which has a puzzlingly low nightside flux in 4.5μm (Knutson et al., 2012; Steinrueck et al., 2019). The lack of irradiation on the nightside may have prevented photodissociation of the molecule, and the lower temperatures would be indicative of PH_3 accounting for most of the atmospheric phosphorus budget (Visscher et al., 2006). Even if photodissociated on the dayside, Phosphorus might recombine into Phosphine on the nightside, after being transported by winds. .

Alternative explanations were made for this low $4.5\mu m$ flux. For instance, Carbon monoxide (CO) also has a deep absorption feature in the 4.5μm band (Sharp & Burrows, 2007), and when the phase curve for HD 189733b was first observed in *Spitzer*'s Channel 2, the low nightside

flux was attributed to this molecule (Knutson et al., 2012). It was initially thought that non-equilibrium chemistry would be able to explain the fact that CO was the main carbon-bearing molecule, despite the low temperature. However, recently (Steinrueck et al., 2019) showed that this is not the case: disequilibrium processes alone cannot account for the low fluxes in *Spitzer*'s Channel 2 as excess CO is balanced by a drop in H_2O.

Two other hot Jupiters with similarly low 4.5μm nightside fluxes are HD 209458b (Zellem et al., 2014) and WASP-43b (Stevenson et al., 2017). Here too, models predict they should be significantly brighter than they are in *Spitzer*'s Channel 2, as equilibrium chemistry would point to CH_4 being the main carbon-bearing molecule on the cooler nightside. The inclusion of PH_3 in these models could make revise our understanding of these planets.

Considering PH_3 in atmospheric composition may additionally help to shed light on surprisingly shallow 4.5μm secondary eclipses measured on the daysides of far cooler planets. GJ 436b has had consecutive non-detections in *Spitzer*'s Channel 2 (Stevenson et al., 2010; Lanotte et al., 2014; Morley et al., 2017), pointing to a CO/CH_4 ratio which is considerably higher than equilibrium chemistry would predict for an object of this temperature ($\approx$700K (Turner et al., 2016)). 'Additional absorbers' have been postulated for GJ 436b by Morley et al. (2017) in order to resolve the apparent low flux in this wavelength, and PH_3 could be that absorber.

A similar non-detection in the 4.5μm band for WASP-29b prompted claims of possible non-equilibrium abundances of CO (Hardin et al., 2012). WASP-29b is a Saturn-sized object with an equilibrium temperature of 980K; PH_3 could yet again provide an explanation for this excess absorption. Most recently, GJ 3470b had a minute 4.5μm flux measured by Benneke et al. (2019); this is a low metallicity, sub-Neptune sized planet with an equilibrium temperature of approximately 600K. Equilibrium chemistry once again points to Methane accounting for most of its atmospheric carbon budget, and Phosphine as an convenient molecule to explain the observations.

4.2   Upcoming Missions

The *James Webb* Space Telescope (*JWST*) is scheduled for launch in 2021 and is intended as a successor to the *Hubble* Space Telescope. A recent simulation of *JWST* spectra by Wang et al. (2017) assessed the detectability of PH_3 by the telescope's NIRCam instrument and found that it would be detectable in emission for objects of around 500K. Although they concluded that for objects of 1000K or more PH_3 could not be resolved, we speculate that objects of intermediate temperatures, such as GJ 436b, might have detectable PH_3 due to their low $4.5\mu m$ fluxes. Additionally, the MIRI instrument will cover the wavelength range of *Spitzer*'s $5.8\mu m$ band (Rieke et al., 2015); we can therefore use photometry taken in this instrument's Channel 1 to add objects highlighted in Figure 3.4 to our PH_3 diagnostic colour-magnitude diagram. The extent to which these objects are offset from the brown dwarfs will indicate whether we should follow up on them using NIRCam to search for PH_3.

JWST will also be equipped with a Near Infrared Spectrograph [REF] (NIRSpec) with wavelength coverage of 0.6–5.3μm. We will therefore be able to use our photometry tools to make diagnostics about the planets' atmospheres, using colour-magnitude diagrams by integrating *JWST* spectra. While this does not replace a full atmospheric retrieval, the goal will be to identify objects that appear to be, for instance carbon-rich, or outlying the main population for one reasons or other, and propose them for a more detailed follow-up as was simulated by Schlawin et al. (2018).

The C/O ratio is essential to our understanding of how and where a planet formed (e.g. Madhusudhan et al., 2011b; Madhusudhan, 2012; Madhusudhan et al., 2017). It can also tell us whether or not a thermal inversion is likely, as carbon-rich atmospheres favour low abundances of the two molecules thought to be producing inversions (Madhusudhan & Seager, 2011): TiO and VO (Fortney et al., 2008). Additionally, the C/O ratio can give an indication about the habilitability of a planet (Johnson et al., 2015), as a C/O$\geq$1 causes depletion of water, even if the planet is within the habitable zone.

The detailed spectra which *JWST* will be capable of producing will also help to shed light

on the atmospheres of controversial planets such as WASP-12b. This planet is predicted to have a stratosphere due to its very hot temperature (Hebb et al., 2009); however, so far TiO and VO have not been detected with any certainty as measurements of eclipse depths in relevant bands have been inconsistent (Sing et al., 2013; Hooton et al., 2019). Most recently, there has been close scrutiny of the orbit of WASP-12b due to the changing transit mid-points; the data now available points to orbital decay over apsidal precession (Bailey & Goodman, 2019; Yee et al., 2020). There is also no consensus as yet on whether WASP-12b is carbon- or oxygen-rich: detections of water in transmission (Kreidberg et al., 2015) point to an oxygen-rich atmosphere, yet the shallow 4.5μm eclipse depth indicates CO in absorption rather than emission (Stevenson et al., 2014b).

If WASP-12b does have a thermal inversion caused by TiO, VO or another mechanism, then its position on Figures 3.8 and 3.9 might be misleading. Parmentier et al. (2018) explains how the dissociation of H_2O in the atmospheres of ultra-hot Jupiters with stratospheres leads to free hydrogen atoms capturing electrons. The resulting H^- ions produce absorption features in the same spectral region as H_2O, which can lead to confusion when interpreting low-resolution spectra in the 1.4μm band. In the era of *JWST*, we will be able to refine our interpretations of positions of ultra-hot Jupiters on our colour-magnitude diagrams in order to improve our use of them as diagnostic tools.

Looking further into the future, *ARIEL* (Atmospheric Remote-sensing Exoplanet Large-survey) is planned for launch in 2028. Like *JWST*, it will be equipped with near- and mid-infrared spectrographs which will allow for detailed atmospheric characterisation[1]. In particular, the Near Infrared Spectrograph (NIRSpec) covers the wavelength ranges of the H and W_{JH} bands which will enable us to get an initial diagnostic on the C/O ratio, while the IR spectrograph covers the 1.95–7.8μm range allowing us to choose targets to follow-up on to find PH_3.

Edwards et al. (2019) recently produced a list of potential targets for *ARIEL* along with their radii and equilibrium temperatures. We searched the literature for their surface gravities, host star metallicities and host star spectral types; we were able to find all three data for 210 of

---

[1]https://ARIELspacemission.files.wordpress.com/2017/05/ARIEL-ral-pl-dd-001_ARIEL-payload-design-description_iss-2-01.pdf
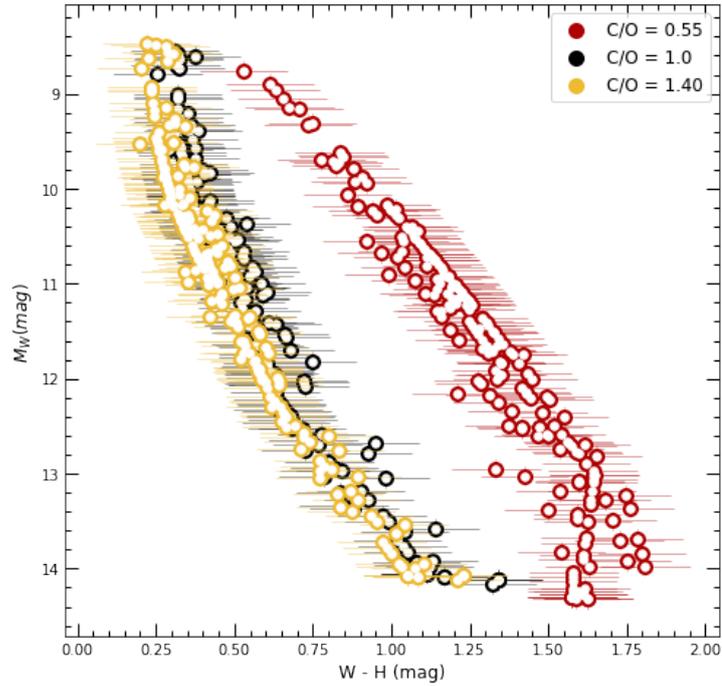
Figure 4.1: Simulation of the *ARIEL* yield on a colour-magnitude diagram of $M_{W_{JH}}$ vs. $[W_{JH} - H]$, plotted using our function `CMD_model`. The closest matching model spectrum was selected for each and plotted with a C/O value of 0.55, 1.0 and 1.40 to show the spread in colour. Points are coloured according to C/O ratio.

the potential targets. We used this information to select the most appropriate model spectrum from Mollière et al. (2015) and plotted them on a M_W vs $[W_{JH}\text{-}H]$ colour-magnitude diagram, assigning C/O ratio values of 0.55, 1 and 1.40. As the Mollière models are only available in 250K increments, we interpolated the magnitudes in order to get a more realistic spread of colours. Are we didn't have access to the *ARIEL* Radiometric Model (Mugnai et al., 2019) to estimate the true errors, we assigned an error of ±1 mag. This choice was not arbitrary; when computing photometry from HST/WFC3 spectra, the data with resolution comparable to what *ARIEL* will produce yielded signal-to-noise ratio of 10, equivalent to a tenth of a magnitude. We present the resulting plot in Figure 4.1 .

While the values for surface gravity, metallicity and host star spectral type had to be rounded to fit the model grid, we can see that objects with C/O ratio ≥1 are distinguishable from oxygen-rich objects.
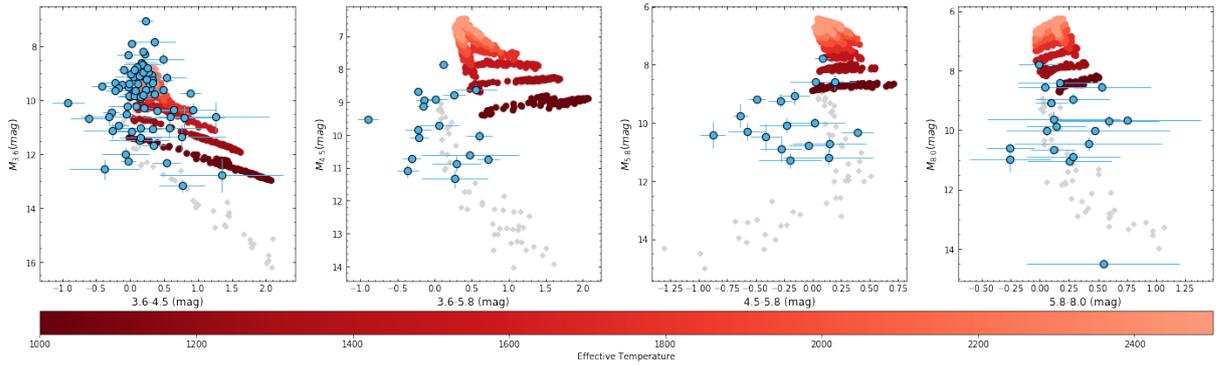
Figure 4.2: Colour-magnitude diagrams in *Spitzer* channels 1–4. Planetary magnitudes are not adjusted as we want to show how closely they match with model atmospheres. Model points are coloured according to effective temperature.

4.3 Model Calibrations

Our C/O ratio diagnostic tools rely on the availability and reliability of model spectra. We chose to use the models presented in Mollière et al. (2015) as they covered a very wide parameter space and were publicly available. However, those models have limitations which impact the validity of our inferences.

The first limitation we find is simply the range of temperatures available. *JWST* and *ARIEL* will both observe objects cooler than 1000K in more detail than ever before, and in order to use models to characterise these objects it is essential that we have model spectra in this temperature range.

The second limitation comes from the quality of the fit for different wavelengths. In their paper, Mollière et al. (2015) showed a comparison between their retrieved model spectrum for HD-179833b and the many thermal emission measurements available for this planet. They showed that *Spitzer* photometry at 8μm was well fit by their model, while the shorter wavelength channels were not. They also showed that while the pattern for the HST data was well fit, the measured eclipse depths were larger than those retrieved by the model.

We illustrate the disparity between the measured data and the model spectra in IRAC channels in Figure 4.2. It is clear from these plots that there is a systematic offset in all four *Spitzer* bands when we compare with a large enough sample. But this also demonstrates that colour-magnitude diagrams, and indeed our tools to produce them, are especially valuable to modellers to validate

46

their model spectra. It is also a cautionary note since similar spectra used for retrieval would be unlikely to lead to correct abundances.

The completeness of the chemistry included into the models impacts the outcome of retrievals. In particular, Baudino et al. (2017) showed how an incomplete line list for PH_3, let alone its exclusion from models altogether, can lead to this crucial molecule not being detected at all. We would also need oxides of titanium and vanadium included in radiative transfer calculations in order to ensure that possible thermal inversions are explored.

5   CONCLUSIONS

Each of the conclusions listed in this chapter has been expanded on from the versions which will appear in the paper on which I will be first author.

This thesis has presented a public Python toolkit for the plotting of near- and mid-infrared colour-magnitude diagrams. To demonstrate the functionality of the toolkit, and the usefulness of colour-magnitudes of transiting exoplanets, we have presented a selection of our newly plotted diagrams. From these we have identified some trends:

- Two objects (HAT-P-2b and GJ 436b) are very blue in [3.6μm - 5.8μm] colour. Despite the fact that for each of these planets the blue colour is caused by excess emission in different bands, what they have in common is high eccentricity. Further follow-up could reveal if their colours are related to their eccentricity, and if so, whether mass and eccentricity are linked to cause excess brightness in different photometric bands. Remeasuring the mid-infrared photometry of XO-3b will also confirm why this planet does not share the blue colours of HAT-P-2b and GJ 436b. We also identified WASP-65b as an outlier in colour; this planet appears to be distinct from other hot Jupiters only in its abnormally high density. Follow-up on all of these planets would allow us to disentangle which of these effects are truly caused by anomalies in the systems rather than the nature of the measurements.

- Objects cooler than 1000K show a wide spread in colours in [3.6μm - 4.5μm] colour, which could be attributed to mass, metallicity and C/O ratio. By comparing the positions of five planets to the colours of model atmospheres we find that for C/O ratio $\geq$0.85, high metallicity causes reddening. At C/O ratios $\leq$0.75, increasing metallicity causes

increasing blueness. For the planets we plotted, we also find that increasing surface gravity corresponds to redder colours. With the onset of a new age of telescopes capable of high resolution spectroscopy of such cool objects, detailed characterisation of planets close to the T spectral class will soon be possible.

- We attribute the comparative blueness of planets in [4.5μm - 5.8μm] colour to missing PH$_3$, which absorbs prominently in the 4.5μm band. Field brown dwarfs in this temperature range could be expected to have hosphine account for most of their atmospheric phosphurus budget, yet as PH$_3$ is susceptible to photolysis by ultraviolet radiation, we believe it is feasible that hot and ultra-hot Jupiters would be missing this absorber. We propose that PH$_3$ might have been overlooked, and could help explain several low 4.5μm fluxes, including on the dayside of GJ 436b and the nightside of HD 189733b.

- The [W_{JH}-H] colour index can be used to diagnose the C/O ratio of exoplanets. Magnitude increases in the W-band with increased water absorption, which we attribute to lower C/O ratios. From its position on a M$_{W_{JH}}$ vs [W_{JH}-H] diagram, we find thay WASP-12b coincides with a carbon-rich model atmosphere. While this is in tension with other results which would attribute its colour to a thermal inversion, we believe there is scope for further investigation to resolve the controversy.

5.1 Where to from here?

This really is a crucial time in the relatively short history of exoplanet science. As a field, it has the ability to capture the imagination of the public and scientific community alike; this in turn means that bright new scientific minds and unprecedented levels of funding are being directed at the search for new worlds. Our toolkit is simple enough that astronomers new to the field can use it with ease, but sophisticated enough to produce plots which allow valuable scientific inferences to be drawn.

The next steps would require refinement of the constraints we can derive from model atmospheres on colour-magnitude diagrams. In order for this to happen, model spectra need to

be calibrated to real data to the greatest extent possible. Our colour-magnitude diagrams are very well suited to this purpose and a measurable offset can be observed on our plots. Additionally, if more modellers make their spectra public, we can include a variety of model grids in order to show the impact of including different chemistry.

With the launch of *JWST* now tantalisingly close, our colour-magnitude diagrams will be an invaluable tool for target selection in this new era of exoplanet atmospheric characterisation.

A   PLANET DATABASE

In these tables we present the planetary databases. Table A.1 contains eccentricities, radii, equilibrium temperatures, host star spectral types and astrometric distances to planets included in our database. Table A.2 contains secondary eclipse measurements in near- and mid-infrared bands for all planets we have included on our colour-magnitude diagrams. Both tables can be downloaded in .txt or .xlsx form from Githib.

Planet	Eccentricity	Radius (R_J)	Equilibrium Temperature (K)	Host Star Spectral Type	Distance (pc)	References
CoRoT-1 b	0	1.49±0.08	1898±50	G0 V	787.91±24.18	19 14
CoRoT-2 b	0.0143±0.0077	$1.466^{+0.042}_{-0.044}$	1521±18	G7V	213.28±2.49	94 225 14 197
GJ 3470 b	0.017±0.016	0.408±0.016	594±97	M1.5	29.42±0.05	29 13 32 14
GJ 436 b	0.13827±0.00018	0.372±0.015	686±10	M2.5 V	9.75±0.01	150 248 38 14
HAT-P-1 b	0	1.319±0.019	1322^{+14}_{-15}	G0 V	158.98±0.98	170 181 121 14
HAT-P-13 b	0.0133±0.0041	1.272±0.065	1740±27	G4	246.81±2.23	261 248 16 14
HAT-P-18 b	0.084±0.048	0.995±0.052	852±28	K2	161.4±0.61	102 14
HAT-P-19 b	0.067±0.042	1.132±0.072	1010±42	K1	202.08±1.47	102 14
HAT-P-2 b	0.5172±0.0019	$0.951^{+0.039}_{-0.053}$	1540±30	F8	127.77±0.43	170 142 188 14
HAT-P-20 b	0.015±0.005	0.867±0.033	970±23	K3	71.04±0.2	17 14
HAT-P-23 b	0.11±0.04	1.09±0.23	1951±30	G0	364.81±4.77	229 52 17 14
HAT-P-3 b	0	0.94±0.07	1189±16	K	134.55±0.48	229 225 239 14
HAT-P-30 b	0.04±0.02	1.44±0.15	1630±42	F7	213.99±2.22	229 123 144 14
HAT-P-32 b	$0.159^{+0.051}_{-0.028}$	1.98±0.045	1836±7	-	289.21±5.35	256 14
HAT-P-33 b	0	1.85±0.49	1782±28	F4	396.11±7.65	229 103 144 14
HAT-P-4 b	0	$1.274^{+0.049}_{-0.06}$	1686^{+30}_{-26}	G1 V	320.45±2.85	240 132 14
HAT-P-40 b	0	1.52±0.17	1770±33	F	464.47±6.54	229 104 14
HAT-P-41 b	0	2.05±0.5	1941±38	F	348.18±4.53	229 104 14
HAT-P-6 b	0	1.48±0.15	1675^{+32}_{-31}	F8 V	275.36±3.64	229 240 14 84
HAT-P-7 b	0	1.51±0.21	2733±21	F6 V	341.08±2.43	229 175 14 84
HAT-P-8 b	0	1.4±0.13	1700±35	F6	211.55±1.71	229 137 144 14
HD 149026 b	0	0.74±0.02	1626^{+69}_{-37}	G0	75.86±0.17	229 223 40 14
HD 189733 b	0	1.13±0.01	1209±11	K2 V	19.76±0.01	229 2 98 14
HD 209458 b	0	1.39±0.02	1459±12	F8	48.3±0.12	229 223 40 14
KELT-1 b	$0.0099^{+0.01}_{-0.0069}$	$1.11^{+0.032}_{-0.022}$	-	F5	268.43±3.06	216 14
KELT-2 A b	0	1.35±0.08	-	F8	134.06±0.8	229 40 14
KELT-3 b	0	1.56±0.11	1816^{+37}_{-39}	F	210.25±5.54	229 190 14
KELT-7 b	0	1.6±0.06	2048±27	F	136.68±0.94	229 30 14
Kepler-13A b	$0.00064^{+0.00012}_{-0.00016}$	1.512±0.035	2550±80	A	519.1±30.7	80 14 212
Kepler-5 b	0.043	$1.426^{+0.036}_{-0.051}$	1750±20	F5V	899.78±16.77	33 80 14 86
Kepler-6 b	0.06	$1.304^{+0.018}_{-0.033}$	1460±10	-	587.04±5.07	33 80 14
Qatar-1 b	0	$1.143^{+0.028}_{-0.025}$	1418^{+28}_{-27}	K	185.62±0.8	55 14 7
TrES-1 b	0	1.13±0.06	1140^{+13}_{-12}	K0 V	159.66±0.74	229 240 5 14
TrES-2 b	0	1.36±0.08	1466±9	G0 V	215.32±1.05	229 187 182 14
TrES-3 b	0	$1.336^{+0.031}_{-0.037}$	1638±22	G4 V	231.34±1.3	228 224 183 14

52

TrES-4 b	0	1.61±0.18	1778±22	F8 V	515.98±7.03	229 248 162 14
WASP-1 b	0	$1.483^{+0.024}_{-0.034}$	1812±14	F7 V	393.07±10.8	149 248 54 14
WASP-10 b	$0.0473^{+0.0034}_{-0.0029}$	1.08±0.02	1370±50	K5 V	141±0.75	130 122 207 14
WASP-100 b	0	1.33±0.14	2190±140	F2	364.41±2.75	229 109 14
WASP-101 b	0	1.43±0.09	1560±35	F6	201.22±1.15	229 109 14
WASP-103 b	0.15	$1.528^{+0.073}_{-0.047}$	2508^{+75}_{-70}	F8 V	883.3±120.5	33 96 14
WASP-104 b	0	1.137±0.037	1516±39	G8	185.93±1.48	220 14
WASP-12 b	0.0447	1.937±0.056	2593±57	G0 V	427.25±6.07	248 43 14
WASP-121 b	0	1.865±0.044	2358±52	F6 V	269.9±1.58	67 14
WASP-131 b	0	1.22±0.05	1460±30	G0	200.08±2.66	111 14
WASP-14 b	0.09	1.38±0.08	1872±29	F5V	162±0.81	229 199 14 77
WASP-17 b	0	1.87±0.24	1755±28	F4	405.91±8.78	229 226 244 14
WASP-18 b	0	1.191±0.038	2413±44	F6 IV	123.48±0.37	229 213 117 14
WASP-19 b	$0.002^{+0.014}_{-0.002}$	1.392±0.04	2520	G8 V	268.33±1.72	264 106 14
WASP-2 b	$0.0054^{+0.009}_{-0.0044}$	$1.081^{+0.041}_{-0.04}$	1311^{+52}_{-50}	K1 V	153.24±1.64	130 2 54 14
WASP-24 b	0	1.38±0.16	1772±29	F8/9	322.11±4.5	229 227 14 77
WASP-26 b	0	1.21±0.15	1650±24	G0	252.76±4.76	229 227 14 77
WASP-3 b	0	1.42±0.17	2020±35	F7 V	231.16±1.65	229 224 14 194
WASP-33 b	0	1.593±0.074	2782±41	A5	121.94±1	229 43 40 14
WASP-36 b	0.019	1.327±0.021	1733±19	G2	386.35±5.26	33 160 14 218
WASP-39 b	0	1.27±0.04	1166±14	G	213.98±1.76	83 161 14 251
WASP-4 b	0	1.321±0.039	1673±17	G7 V	267.21±3.77	34 225 259 14
WASP-43 b	0	$0.93^{+0.07}_{-0.09}$	1427±9	K7 V	86.75±0.33	107 79 207 14
WASP-46 b	0.022	1.174±0.037	1636±44	G6 V	375.31±4.46	33 53 53 14
WASP-48 b	0	1.5±0.2	2035±52	G	454.14±4.47	229 248 14
WASP-5 b	$0.038^{+0.026}_{-0.018}$	$1.087^{+0.068}_{-0.071}$	1706^{+52}_{-48}	G4 V	309.14±3.41	93 8 14
WASP-6 b	0.05	1.03±0.1	1184±16	G8 V	197.12±1.63	229 242 14
WASP-62 b	0	1.32±0.08	1475^{+25}_{-20}	F7	175.63±0.59	229 36 14 108
WASP-63 b	0	1.41±0.14	-	G8	290.68±2.03	229 14 108
WASP-64 b	0	1.271±0.039	1689±49	G7	369.93±3.03	95 14
WASP-65 b	0	1.112±0.059	1480±10	G6	273.7±2.73	97 14
WASP-67 b	0	1.15±0.11	1003±20	K0 V	189.47±1.56	229 159 14 108
WASP-69 b	0	1.11±0.04	963±18	K5	49.96±0.13	229 41 12 14
WASP-74 b	0	1.36±0.1	1910±40	F9	149.22±1.15	229 110 14
WASP-76 b	0	$1.83^{+0.06}_{-0.04}$	2160±40	F7	194.46±6.21	257 14
WASP-77 A b	0	1.38±0.09	1674±24	G8 V	105.17±1.21	229 248 165 14

WASP-78 b	0	1.93±0.45	2470$^{+54}_{-56}$	F8	754.26±17.1	229 36 14 217
WASP-79 b	0	1.67±0.15	1716$^{+26}_{-24}$	F5	246.69±1.82	229 36 14 217
WASP-8 b	0.31	1.13±0.05	-	G8 V	89.96±0.36	229 207 14
WASP-80 b	0.002$^{+0.01}_{-0.002}$	0.999$^{+0.03}_{-0.031}$	825±19	K7 V	49.79±0.12	247 245 14
WASP-87 b	0	1.385±0.06	-	F5	298.39±3.62	1 14 11
WASP-94 A b	0	1.58±0.13	1604$^{+25}_{-22}$	F8	211.21±2.51	229 180 14
WASP-97 b	0	1.14±0.06	1555±40	G5	151.07±0.51	229 109 14
XO-1 b	0	1.14±0.07	1210±16	G1 V	163.55±0.62	229 223 167 14
XO-2 N b	0.028$^{+0.038}_{-0.022}$	0.993±0.012	1328$^{+17}_{-28}$	K0 V	154.27±1.46	130 60 225 37 14
XO-3 b	0.29	1.41±0.12	1729±34	F5 V	213.05±2.72	229 223 120 14
XO-4 b	0	1.25±0.08	1630$^{+169}_{-36}$	F5 V	272.65±2.91	229 223 168 14

Table A.1: Composite planet data which we have used in this thesis. Compiled with the help of the NASA Exoplanet Archive.

54

Planet	J	H	K	$3.6\mu m$	$4.5\mu m$	$5.8\mu m$	$8.0\mu m$	W_{JH}	References
CoRoT-1 b	-	0.145±0.049	0.336±0.042	0.415±0.042	0.482±0.042	-	-	-	270 204 69
CoRoT-2 b	-	-	0.16±0.09	0.355±0.02	0.5±0.02	-	0.51±0.059	-	6 69
GJ 3470 b	-	-	-	$0.0115^{+0.0027}_{-0.0026}$	0.0003±0.0022	-	-	-	28
GJ 436 b	-	-	0.109±0.025	0.041±0.003	-	0.033±0.014	0.054±0.008	-	231
HAT-P-1 b	-	-	-	0.08±0.008	0.135±0.022	0.203±0.031	0.238±0.04	-	274 236
HAT-P-13 b	-	-	-	0.0801±0.0081	0.19±0.0124	-	-	-	101 92
HAT-P-18 b	-	-	-	$0.0437^{+0.0146}_{-0.0144}$	$0.0326^{+0.0144}_{-0.0147}$	-	-	-	253
HAT-P-19 b	-	-	-	0.062±0.014	0.062±0.016	-	-	-	126
HAT-P-2 b	-	-	-	0.0996±0.0072	0.1031±0.0061	$0.071^{+0.029}_{-0.013}$	$0.1392^{+0.0095}_{-0.0095}$	-	139
HAT-P-20 b	-	-	-	0.0615±0.0082	0.1096±0.0077	-	-	-	71
HAT-P-23 b	-	-	0.234±0.046	0.248±0.019	0.309±0.026	-	-	-	185 185
HAT-P-3 b	-	-	-	$0.112^{+0.015}_{-0.03}$	$0.094^{+0.016}_{-0.009}$	-	-	-	238
HAT-P-30 b	-	-	-	0.1584±0.0107	0.1825±0.0147	-	-	-	92
HAT-P-32 b	0.04±0.014	0.09±0.033	0.178±0.057	0.364±0.016	0.438±0.02	-	-	0.051±0.013	this work 271
HAT-P-33 b	-	-	-	0.1603±0.0127	0.1835±0.0199	-	-	-	92
HAT-P-4 b	-	-	-	$0.142^{+0.014}_{-0.016}$	$0.122^{+0.012}_{-0.014}$	-	-	-	238
HAT-P-40 b	-	-	-	0.0988±0.0168	0.1057±0.0145	-	-	-	92
HAT-P-41 b	-	-	-	0.1829±0.0319	0.2278±0.0177	-	-	-	92
HAT-P-6 b	-	-	-	0.117±0.008	0.106±0.006	-	-	-	237
HAT-P-7 b	-	-	-	0.098±0.017	0.159±0.022	0.245±0.031	0.262±0.027	-	51
HAT-P-8 b	-	-	-	$0.131^{+0.007}_{-0.01}$	$0.111^{+0.008}_{-0.007}$	-	-	-	237
HD 149026 b	-	-	-	0.04±0.003	0.034±0.006	0.044±0.01	0.052±0.006	-	232
HD 189733 b	-	-	-	0.256±0.014	0.214±0.02	0.31±0.034	$0.344^{+0.0036}_{-0.0036}$	-	46
HD 209458 b	0.091±0.018	-	-	$0.106^{+0.007}_{-0.008}$	0.133±0.011	$0.142^{+0.059}_{-0.058}$	0.215±0.012	0.073±0.018	this work 81
KELT-1 b	-	-	$0.16^{+0.018}_{-0.02}$	0.195±0.01	0.2±0.012	-	-	-	59 25
KELT-2 A b	-	-	-	$0.0572^{+0.0045}_{-0.0046}$	$0.0616^{+0.0044}_{-0.0045}$	-	-	-	192
KELT-3 b	-	-	-	0.1766±0.0097	0.1656±0.0104	-	-	-	92
KELT-7 b	-	-	-	0.1688±0.0046	0.1896±0.0057	-	-	-	92
Kepler-13 Ab	0.0724±0.0071	-	0.122±0.051	0.156±0.031	0.222±0.023	-	-	0.071±0.08	this work 212
Kepler-5 b	-	-	-	0.103±0.017	0.107±0.015	-	-	-	73
Kepler-6 b	-	-	-	0.069±0.027	0.151±0.019	-	-	-	73
Qatar-1 b	-	-	0.136±0.034	0.149±0.051	0.273±0.049	-	-	-	59 91
TrES-1 b	-	-	-	0.083±0.024	0.094±0.024	0.162±0.042	0.213±0.042	-	63
TrES-2 b	-	-	$0.062^{+0.013}_{-0.011}$	0.127±0.021	0.23±0.024	0.199±0.054	0.359±0.06	-	56 184
TrES-3 b	-	-	$0.133^{+0.018}_{-0.016}$	0.356±0.035	0.372±0.054	0.449±0.097	0.475±0.046	0.047±0.028	57 87

Planet								Ref.
TrES-4 b	-	-	0.137±0.011	0.148±0.016	0.261±0.059	0.318±0.044	-	128
WASP-1 b	-	-	0.184±0.016	0.217±0.017	0.274±0.058	0.474±0.046	-	258
WASP-10b	-	$0.137^{+0.013}_{-0.019}$	0.1±0.011	0.146±0.016	-	-	-	61 126
WASP-100	-	-	0.1267±0.0098	0.172±0.0119	-	-	-	92
WASP-101	-	-	0.1161±0.0111	0.1194±0.0113	-	-	-	92
WASP-103 b	0.131±0.02	$0.3567^{+0.04}_{-0.035}$	0.3702±0.0256	0.4711±0.0339	-	-	0.146±0.027	this work 68 92
WASP-104 b	-	-	0.1709±0.0195	0.2643±0.0303	-	-	-	92
WASP-12 b	0.139±0.03	0.296±0.014	0.421±0.011	0.428±0.012	0.696±0.06	0.696±0.096	0.198±0.022	this work 58 59 234
WASP-121 b	0.107±0.011	$0.176^{+0.016}_{-0.021}$	0.367±0.013	0.4684±0.0121	-	-	0.125±0.011	this work 82 92
WASP-131 b	-	-	0.0364±0.0097	0.0282±0.0078	-	-	-	92
WASP-14 b	-	-	0.1816±0.0067	0.2284±0.009	-	0.181±0.022	-	92
WASP-17 b	-	-	-	0.229±0.013	-	0.237±0.039	-	9
WASP-18 b	0.094±0.004	0.13±0.03	0.2973±0.007	0.3858±0.0113	0.37±0.03	0.41±0.02	0.108±0.004	this work 273 211
WASP-19 b	-	0.276±0.044	0.287±0.02 / 0.483±0.025	0.572±0.03	0.65±0.11	0.73±0.12	-	10 272 10
WASP-2 b	-	-	0.083±0.035	0.169±0.017	0.192±0.077	0.285±0.059	-	258
WASP-24 b	-	-	0.159±0.013	0.202±0.018	-	-	-	219
WASP-26 b	-	-	0.126±0.013	0.149±0.016	-	-	-	158
WASP-3 b	-	0.193±0.014	$0.209^{+0.04}_{-0.028}$	0.282±0.012	-	$0.328^{+0.086}_{-0.055}$	-	59 205
WASP-33 b	0.11±0.03	$0.244^{+0.027}_{-0.02}$	0.26±0.05	0.41±0.02	-	-	0.123±0.025	this work 275 70
WASP-36 b	-	0.13±0.04	-	-	-	-	-	273
WASP-39 b	-	-	0.088±0.015	0.096±0.018	-	-	-	126
WASP-4 b	-	$0.185^{+0.014}_{-0.013}$	0.319±0.031	0.343±0.027	-	-	-	39 26
WASP-43 b	0.042±0.0045	0.194±0.029	0.3773±0.0138	0.3866±0.0195	-	-	0.036±0.004	this work 254 92
WASP-46 b	0.129±0.055	$0.26^{+0.05}_{-0.03}$	0.136±0.0701	0.4446±0.0589	-	-	-	49 273 92
WASP-48 b	0.047±0.016	0.109±0.027	0.176±0.013	0.214±0.02	-	-	-	185 185
WASP-5 b	$0.168^{+0.05}_{-0.052}$	0.2±0.02	0.197±0.028	0.237±0.024	-	-	-	48 273 21
WASP-6 b	-	-	0.094±0.019	0.115±0.022	-	-	-	126
WASP-62 b	-	-	0.1616±0.0146	0.1359±0.013	-	-	-	92
WASP-63 b	-	-	0.0522±0.0095	0.0533±0.0128	-	-	-	92
WASP-64 b	-	-	0.2859±0.027	0.2071±0.0471	-	-	-	92
WASP-65 b	-	-	0.1587±0.0245	0.0724±0.0318	-	-	-	92
WASP-67 b	-	-	0.022±0.013	0.08±0.018	-	-	-	126
WASP-69 b	-	-	0.0421±0.0029	0.0463±0.0039	-	-	-	253
WASP-74 b	-	-	0.1446±0.0066	0.2075±0.01	-	-	-	92
WASP-76 b	-	-	0.2645±0.0063	0.3345±0.0082	-	-	-	92
WASP-77 b	-	-	0.1845±0.0094	0.2362±0.0127	-	-	-	92

Table A.2 continued from previous page

WASP-78 b	-	0.2001±0.0218	0.2013±0.0351	-	-	-	92
WASP-79 b	-	0.1394±0.0088	0.1783±0.0106	-	-	-	92
WASP-8 b	-	0.113±0.018	0.0692±0.0068	-	0.093±0.023	-	62
WASP-80 b	-	0.455±0.1	0.944±0.064	-	-	-	247
WASP-87 b	-	0.2077±0.0127	0.2705±0.0137	-	-	-	92
WASP-94A b	-	0.0867±0.0059	0.0995±0.0093	-	-	-	92
WASP-97 b	-	0.1359±0.0084	0.1534±0.0101	-	-	-	92
XO-1 b	-	0.086±0.007	0.122±0.009	0.261±0.031	0.21±0.029	-	146
XO-2 N b	-	0.081±0.017	0.098±0.02	0.167±0.036	0.133±0.049	-	147
XO-3 b	-	0.101±0.004	0.158±0.0036	0.134±0.049	0.15±0.036	-	148 263
XO-4 b	-	$0.056^{+0.012}_{-0.006}$	0.135±0.01	-	-	-	237

Table A.2: Planet secondary eclipse measurements in near- and mid-infrared bands, including our W_{JH} band.

Bibliography

Addison B. C., Tinney C. G., Wright D. J., Bayliss D., 2016, ApJ, 823, 29

Addison B., et al., 2019, PASP, 131, 115003

Allard F., Hauschildt P. H., Alexander D. R., Tamanai A., Schweitzer A., 2001, ApJ, 556, 357

Alonso R., 2018, Characterization of Exoplanets: Secondary Eclipses. p. 40, doi:10.1007/978-3-319-55333-7_40

Alonso R., et al., 2004, ApJ, 613, L153

Alonso R., Deeg H. J., Kabath P., Rabus M., 2010, AJ, 139, 1481

Alsubai K. A., et al., 2011, MNRAS, 417, 709

Anderson D. R., et al., 2008, MNRAS, 387, L4

Anderson D. R., et al., 2011, MNRAS, 416, 2108

Anderson D. R., et al., 2013, MNRAS, 430, 3422

Anderson D. R., et al., 2014a, arXiv e-prints, p. arXiv:1410.3449

Anderson D. R., et al., 2014b, MNRAS, 445, 1114

Awiphan S., et al., 2016, MNRAS, 463, 2574

Bailer-Jones C. A. L., Rybizki J., Fouesneau M., Mantelet G., Andrae R., 2018, AJ, 156, 58

Bailey A., Goodman J., 2019, MNRAS, 482, 1872

Bakos G. Á., et al., 2009, ApJ, 707, 446

Bakos G. Á., et al., 2011, ApJ, 742, 116

Baraffe I., Chabrier G., Barman T. S., Allard F., Hauschildt P. H., 2003, A&A, 402, 701

Barge P., et al., 2008, A&A, 482, L17

Baruteau C., Masset F., 2013, Recent Developments in Planet Migration Theory. p. 201, doi:10.1007/978-3-642-32961-6_6

Baskin N. J., et al., 2013, ApJ, 773, 124

Batista V., 2018, Finding Planets via Gravitational Microlensing. p. 120, doi:10.1007/978-3-319-55333-7_120

Batygin K., Bodenheimer P. H., Laughlin G. P., 2016, ApJ, 829, 114

Baudino J.-L., Mollière P., Venot O., Tremblin P., Bézard B., Lagage P.-O., 2017, ApJ, 850, 150

Beatty T. G., et al., 2014, ApJ, 783, 112

Beerer I. M., et al., 2011, ApJ, 727, 23

Benneke B., 2015, arXiv e-prints, p. arXiv:1504.07655

Benneke B., et al., 2019, Nature Astronomy, p. 361

Biddle L. I., et al., 2014, MNRAS, 443, 1810

Bieryla A., et al., 2015, AJ, 150, 12

Biller B. A., Bonnefoy M., 2018, Exoplanet Atmosphere Measurements from Direct Imaging. p. 101, doi:10.1007/978-3-319-55333-7_101

Bonfils X., et al., 2012, A&A, 546, A27

Bonomo A. S., et al., 2017, A&A, 602, A107

Bouma L. G., et al., 2019, AJ, 157, 217

Bowler B. P., 2016, PASP, 128, 102001

Brown D. J. A., et al., 2017, MNRAS, 464, 810

Burke C. J., et al., 2007, ApJ, 671, 2115

Butler R. P., Vogt S. S., Marcy G. W., Fischer D. A., Wright J. T., Henry G. W., Laughlin G., Lissauer J. J., 2004, ApJ, 617, 580

Cáceres C., et al., 2011, A&A, 530, A5

Cannon A. J., Pickering E. C., 1918, Annals of Harvard College Observatory, 91, 1

Casasayas-Barris N., Palle E., Nowak G., Yan F., Nortmann L., Murgas F., 2017, A&A, 608, A135

Casewell S. L., et al., 2015, MNRAS, 447, 3218

Chakrabarty A., Sengupta S., 2019, AJ, 158, 39

Charbonneau D., Brown T. M., Latham D. W., Mayor M., 2000, ApJ, 529, L45

Charbonneau D., Brown T. M., Noyes R. W., Gilliland R. L., 2002, ApJ, 568, 377

Charbonneau D., Knutson H. A., Barman T., Allen L. E., Mayor M., Megeath S. T., Queloz D., Udry S., 2008, ApJ, 686, 1341

Chen J., Kipping D., 2017, ApJ, 834, 17

Chen G., et al., 2014a, A&A, 563, A40

Chen G., van Boekel R., Wang H., Nikolov N., Seemann U., Henning T., 2014b, A&A, 567, A8

Chinchilla P., et al., 2020, A&A, 633, A152

Christiansen J. L., et al., 2010, ApJ, 710, 97

Ciceri S., et al., 2015, A&A, 577, A54

Ciceri S., et al., 2016, MNRAS, 456, 990

Collier Cameron A., et al., 2007, MNRAS, 375, 951

Collins K. A., Kielkopf J. F., Stassun K. G., 2017, AJ, 153, 78

Croll B., Albert L., Lafreniere D., Jayawardhana R., Fortney J. J., 2010a, ApJ, 717, 1084

Croll B., Jayawardhana R., Fortney J. J., Lafrenière D., Albert L., 2010b, ApJ, 718, 920

Croll B., Lafreniere D., Albert L., Jayawardhana R., Fortney J. J., Murray N., 2011, AJ, 141, 30

Croll B., et al., 2015, ApJ, 802, 28

Crouzet N., McCullough P. R., Burke C., Long D., 2012, ApJ, 761, 7

Cruz P., Barrado D., Lillo-Box J., Diaz M., Birkby J., López-Morales M., Hodgkin S., Fortney J. J., 2015, A&A, 574, A103

Cubillos P., et al., 2013, ApJ, 768, 42

Cubillos P., Harrington J., Madhusudhan N., Foster A. S. D., Lust N. B., Hardy R. A., Bowman M. O., 2014, ApJ, 797, 42

Cutri R. M., et al. 2012, VizieR Online Data Catalog, p. II/311

Cutri R. M., et al., 2003, VizieR Online Data Catalog, p. II/246

D'Angelo G., Lissauer J. J., 2018, Formation of Giant Planets. p. 140, doi:10.1007/978-3-319-55333-7_140

Delrez L., et al., 2016, MNRAS, 458, 4025

Delrez L., et al., 2018, MNRAS, 474, 2334

Deming D., et al., 2011, ApJ, 726, 95

Deming D., et al., 2012, ApJ, 754, 106

Deming D., et al., 2015, ApJ, 805, 132

Deming D., Louie D., Sheets H., 2019, PASP, 131, 013001

Désert J.-M., et al., 2011, ApJS, 197, 11

Dupuy T. J., Liu M. C., 2012, ApJS, 201, 19

Eddington A. S., 1920, The Scientific Monthly, 11, 297

Edwards B., Mugnai L., Tinetti G., Pascale E., Sarkar S., 2019, in EPSC-DPS Joint Meeting 2019. pp EPSC–DPS2019–603

Ehrenreich D., Désert J. M., 2011, A&A, 529, A136

Encrenaz T., Tinetti G., Coustenis A., 2018, Experimental Astronomy, 46, 31

Esposito M., et al., 2017, A&A, 601, A53

Esteves L. J., De Mooij E. J. W., Jayawardhana R., 2015, ApJ, 804, 150

Evans T. M., Aigrain S., Gibson N., Barstow J. K., Amundsen D. S., Tremblin P., Mourier P., 2015, MNRAS, 451, 680

Evans T. M., et al., 2017, Nature, 548, 58

Faedi F., et al., 2011, A&A, 531, A40

Faedi F., et al., 2013, MNRAS, 433, 2097

Fortney J. J., Lodders K., Marley M. S., Freedman R. S., 2008, ApJ, 678, 1419

Frasca A., et al., 2016, A&A, 594, A39

Fressin F., Knutson H. A., Charbonneau D., O'Donovan F. T., Burrows A., Deming D., Mand ushev G., Spiegel D., 2010, ApJ, 711, 374

Gaia Collaboration et al., 2016, A&A, 595, A1

Gaia Collaboration et al., 2018, A&A, 616, A1

Galle J. G., 1846, MNRAS, 7, 153

Garhart E., Deming D., Mandell A., Knutson H., Fortney J. J., 2018, A&A, 610, A55

Garhart E., et al., 2019, arXiv e-prints, p. arXiv:1901.07040

Gillon M., et al., 2009, A&A, 496, 259

Gillon M., et al., 2010, A&A, 511, A3

Gillon M., et al., 2013, A&A, 552, A82

Gillon M., et al., 2014, A&A, 562, L3

Gómez Maqueo Chew Y., et al., 2013, A&A, 559, A36

Gray R. O., Corbally C. J., Garrison R. F., McFadden M. T., Robinson P. E., 2003, AJ, 126, 2048

Hansen C. J., Schwartz J. C., Cowan N. B., 2014, MNRAS, 444, 3632

Hardin M., Harrington J., Stevenson K., Blecic J., Bowman O., Cubillos P., Nymeyer S., Consortium W., 2012, in AAS/Division for Planetary Sciences Meeting Abstracts #44. AAS/Division for Planetary Sciences Meeting Abstracts. p. 200.09

Hardy R. A., et al., 2017, ApJ, 836, 143

Hartman J. D., et al., 2011a, ApJ, 726, 52

Hartman J. D., et al., 2011b, ApJ, 742, 59

Hartman J. D., et al., 2012, AJ, 144, 139

Hebb L., et al., 2009, The Astrophysical Journal, 693, 1920

Hebb L., et al., 2010, ApJ, 708, 224

Hellier C., et al., 2011, A&A, 535, L7

Hellier C., et al., 2012, MNRAS, 426, 739

Hellier C., et al., 2014, MNRAS, 440, 1982

Hellier C., et al., 2015, AJ, 150, 18

Hellier C., et al., 2017, MNRAS, 465, 3693

Henry G. W., Marcy G., Butler R. P., Vogt S. S., 1999, IAU Circ., 7307, 1

Hermes J. J., 2018, Timing by Stellar Pulsations as an Exoplanet Discovery Method. p. 6, doi:10.1007/978-3-319-55333-7_6

Hertzsprung E., 1911, Publikationen des Astrophysikalischen Observatoriums zu Potsdam, 63

Hobbs R., Shorttle O., Madhusudhan N., Rimmer P., 2019, MNRAS, 487, 2242

Hooton M. J., de Mooij E. J. W., Watson C. A., Gibson N. P., Galindo-Guil F. J., Clavero R., Merritt S. R., 2019, MNRAS, 486, 2397

Houk N., 1978, Michigan catalogue of two-dimensional spectral types for the HD stars

Irwin P. G. J., Parmentier V., Taylor J., Barstow J., Aigrain S., Lee G. K. H., Garland R., 2019, arXiv e-prints, p. arXiv:1909.03233

Jacob W. S., 1855, MNRAS, 15, 228

Johns-Krull C. M., et al., 2007, in American Astronomical Society Meeting Abstracts #210. p. 96.05

Johnson J. A., et al., 2008, ApJ, 686, 649

Johnson J. A., Winn J. N., Cabrera N. E., Carter J. A., 2009, ApJ, 692, L100

Johnson J. A., et al., 2011, ApJ, 735, 24

Johnson T. V., Sevin Peckmezci G., Mousis O., Lunine J. I., Madhusudhan N., 2015, in AAS/Division for Planetary Sciences Meeting Abstracts #47. AAS/Division for Planetary Sciences Meeting Abstracts. p. 404.03

Jordán A., et al., 2013, ApJ, 778, 184

Kammer J. A., et al., 2015, ApJ, 810, 118

Kirkpatrick J. D., 2005, Annual Review of Astronomy and Astrophysics, 43, 195

Knutson H. A., Charbonneau D., Burrows A., O'Donovan F. T., Mandushev G., 2009, ApJ, 691, 866

Knutson H. A., et al., 2012, ApJ, 754, 22

Knutson H. A., et al., 2014, ApJ, 785, 126

Konacki M., Torres G., Jha S., Sasselov D. D., 2003, Nature, 421, 507

Kovács G., et al., 2007, ApJ, 670, L41

Kreidberg L., 2018, Exoplanet Atmosphere Measurements from Transmission Spectroscopy and Other Planet Star Combined Light Observations. p. 100, doi:10.1007/978-3-319-55333-7_100

Kreidberg L., et al., 2014, ApJ, 793, L27

Kreidberg L., et al., 2015, ApJ, 814, 66

Lanotte A. A., et al., 2014, A&A, 572, A73

Latham D. W., et al., 2009, ApJ, 704, 1107

Leonard F. C., 1930, Leaflet of the Astronomical Society of the Pacific, 1, 121

Lewis N. K., et al., 2013, ApJ, 766, 95

Lin D. N. C., Bodenheimer P., Richardson D. C., 1996, Nature, 380, 606

Line M. R., Knutson H., Wolf A. S., Yung Y. L., 2014, ApJ, 783, 70

Loeillet B., et al., 2008, A&A, 481, 529

Lovis C., Fischer D., 2010, Radial Velocity Techniques for Exoplanets. pp 27–53

Luo A. L., Zhao Y. H., Zhao G., et al. 2018, VizieR Online Data Catalog, p. V/153

MacDonald R. J., Madhusudhan N., 2017, ApJ, 850, L15

Machalek P., McCullough P. R., Burke C. J., Valenti J. A., Burrows A., Hora J. L., 2008, ApJ, 684, 1427

Machalek P., McCullough P. R., Burrows A., Burke C. J., Hora J. L., Johns-Krull C. M., 2009, ApJ, 701, 514

Machalek P., Greene T., McCullough P. R., Burrows A., Burke C. J., Hora J. L., Johns-Krull C. M., Deming D. L., 2010, ApJ, 711, 111

Maciejewski G., et al., 2014a, Acta Astron., 64, 11

Maciejewski G., Niedzielski A., Nowak G., Pallé E., Tingley B., Errmann R., Neuhäuser R., 2014b, Acta Astron., 64, 323

Madhusudhan N., 2012, ApJ, 758, 36

Madhusudhan N., 2018, Atmospheric Retrieval of Exoplanets. p. 104, doi:10.1007/978-3-319-55333-7_104

Madhusudhan N., 2019, arXiv e-prints, p. arXiv:1904.03190

Madhusudhan N., Seager S., 2011, ApJ, 729, 41

Madhusudhan N., et al., 2011a, Nature, 469, 64

Madhusudhan N., Mousis O., Johnson T. V., Lunine J. I., 2011b, ApJ, 743, 191

Madhusudhan N., Bitsch B., Johansen A., Eriksson L., 2017, MNRAS, 469, 4102

Mahtani D. P., et al., 2013, MNRAS, 432, 693

Mancini L., et al., 2014, A&A, 568, A127

Mancini L., Kemmer J., Southworth J., Bott K., Mollière P., Ciceri S., Chen G., Henning T., 2016, MNRAS, 459, 1393

Mancini L., et al., 2018, A&A, 613, A41

Mandushev G., et al., 2007, ApJ, 667, L195

Manjavacas E., et al., 2019, AJ, 157, 101

Marois C., Macintosh B., Barman T., Zuckerman B., Song I., Patience J., Lafrenière D., Doyon R., 2008, Science, 322, 1348

Maxted P. F. L., et al., 2013, PASP, 125, 48

Mayor M., Queloz D., 1995, Nature, 378, 355

McCullough P. R., et al., 2006, ApJ, 648, 1228

McCullough P. R., et al., 2008, arXiv e-prints, p. arXiv:0805.2921

McCullough P. R., Crouzet N., Deming D., Madhusudhan N., 2014, ApJ, 791, 55

Ment K., Fischer D. A., Bakos G., Howard A. W., Isaacson H., 2018, AJ, 156, 213

Mohanty S., Jayawardhana R., Huélamo N., Mamajek E., 2007, ApJ, 657, 1064

Mollière P., van Boekel R., Dullemond C., Henning T., Mordasini C., 2015, ApJ, 813, 47

Mordasini C., 2018, Planetary Population Synthesis. p. 143, doi:10.1007/978-3-319-55333-7_143

Morley C. V., Knutson H., Line M., Fortney J. J., Thorngren D., Marley M. S., Teal D., Lupu R., 2017, AJ, 153, 86

Morris B. M., Mandell A. M., Deming D., 2013, ApJ, 764, L22

Moses J. I., Madhusudhan N., Visscher C., Freedman R. S., 2013a, ApJ, 763, 25

Moses J. I., et al., 2013b, ApJ, 777, 34

Moulton F. R., 1899, AJ, 20, 33

Mugnai L., Edwards B., Papageorgiou A., Pascale E., Sarkar S., 2019, in EPSC-DPS Joint Meeting 2019. pp EPSC–DPS2019–270

Neveu-VanMalle M., et al., 2014, A&A, 572, A49

Nikolov N., et al., 2014, MNRAS, 437, 46

O'Donovan F. T., et al., 2006, ApJ, 651, L61

O'Donovan F. T., et al., 2007, ApJ, 663, L37

O'Donovan F. T., Charbonneau D., Harrington J., Madhusudhan N., Seager S., Deming D., Knutson H. A., 2010, ApJ, 710, 1551

O'Rourke J. G., et al., 2014, ApJ, 781, 109

Öberg K. I., Murray-Clay R., Bergin E. A., 2011, ApJ, 743, L16

Öztürk O., Erdem A., 2019, MNRAS, 486, 2290

Pál A., et al., 2010, MNRAS, 401, 2665

Parmentier V., et al., 2018, A&A, 617, A110

Pepper J., et al., 2013, ApJ, 773, 64

Pinhas A., Madhusudhan N., Gandhi S., MacDonald R., 2019, MNRAS, 482, 1485

Piskorz D., et al., 2018, AJ, 156, 133

Planck M., Masius M., 1914, The Theory of Heat Radiation. Blakiston, `http://books.google.co.uk/books?id=2PR_AAAAMAAJ`

Pollacco D., et al., 2008, MNRAS, 385, 1576

Pollack J. B., Hubickyj O., Bodenheimer P., Lissauer J. J., Podolak M., Greenzweig Y., 1996, Icarus, 124, 62

Polyansky O. L., Kyuberis A. A., Zobov N. F., Tennyson J., Yurchenko S. N., Lodi L., 2018, MNRAS, 480, 2597

Poppenhaeger K., Wolk S. J., 2014, A&A, 565, L1

Rackham B. V., Apai D., Giampapa M. S., 2017, in AAS/Division for Planetary Sciences Meeting Abstracts #49. AAS/Division for Planetary Sciences Meeting Abstracts. p. 416.20

Raetz S., et al., 2015, MNRAS, 451, 4139

Rajan A., et al., 2015, ApJ, 809, L33

Rayner J. T., Toomey D. W., Onaka P. M., Denault A. J., Stahlberger W. E., Vacca W. D., Cushing M. C., Wang S., 2003, PASP, 115, 362

Redfield S., Endl M., Cochran W. D., Koesterke L., 2008, ApJ, 673, L87

Rieke G. H., et al., 2015, PASP, 127, 584

Rogers J. C., Apai D., López-Morales M., Sing D. K., Burrows A., 2009, ApJ, 707, 1707

Rostron J. W., Wheatley P. J., Anderson D. R., Collier Cameron A., Fortney J. J., Harrington J., Knutson H. A., Pollacco D. L., 2014, MNRAS, 441, 3666

Russell H. N., 1914, Popular Astronomy, 22, 275

Salz M., Schneider P. C., Czesla S., Schmitt J. H. M. M., 2015, A&A, 576, A42

Schlawin E., Greene T. P., Line M., Fortney J. J., Rieke M., 2018, AJ, 156, 40

Schneider J., Dedieu C., Le Sidaner P., Savalle R., Zolotukhin I., 2011, A&A, 532, A79

Sharp C. M., Burrows A., 2007, ApJS, 168, 140

Sheppard K. B., Mandell A. M., Tamburo P., Gand hi S., Pinhas A., Madhusudhan N., Deming D., 2017, ApJ, 850, L32

Shporer A., et al., 2014, ApJ, 788, 92

Shporer A., et al., 2019, AJ, 157, 178

Sing D. K., et al., 2013, MNRAS, 436, 2956

Sing D. K., et al., 2016, in American Astronomical Society Meeting Abstracts #227. p. 306.03

Siverd R. J., et al., 2012, ApJ, 761, 123

Smalley B., et al., 2012, A&A, 547, A61

Smith A. M. S., et al., 2012a, AJ, 143, 81

Smith A. M. S., et al., 2012b, A&A, 545, A93

Smith A. M. S., et al., 2014, A&A, 570, A64

Sousa-Silva C., Al-Refaie A. F., Tennyson J., Yurchenko S. N., 2015, MNRAS, 446, 2337

Sousa-Silva C., Seager S., Ranjan S., Petkowski J. J., Zhan Z., Hu R., Bains W., 2019, arXiv e-prints, p. arXiv:1910.05224

Southworth J., 2010, MNRAS, 408, 1689

Southworth J., 2011, MNRAS, 417, 2166

Southworth J., 2012, MNRAS, 426, 1291

Southworth J., et al., 2012, MNRAS, 426, 1338

Southworth J., et al., 2014, MNRAS, 444, 776

Sozzetti A., et al., 2009, ApJ, 691, 1145

Stassun K. G., Collins K. A., Gaudi B. S., 2017, AJ, 153, 136

Steinrueck M. E., Parmentier V., Showman A. P., Lothringer J. D., Lupu R. E., 2019, ApJ, 880, 14

Stevenson K. B., et al., 2010, Nature, 464, 1161

Stevenson K. B., et al., 2012, ApJ, 754, 136

Stevenson K. B., et al., 2014a, Science, 346, 838

Stevenson K. B., Bean J. L., Madhusudhan N., Harrington J., 2014b, ApJ, 791, 36

Stevenson K. B., et al., 2017, AJ, 153, 68

Todorov K., Deming D., Harrington J., Stevenson K. B., Bowman W. C., Nymeyer S., Fortney J. J., Bakos G. A., 2010, ApJ, 708, 498

Todorov K. O., et al., 2012, ApJ, 746, 111

Todorov K. O., et al., 2013, ApJ, 770, 102

Torres G., et al., 2007, ApJ, 666, L121

Torres G., Winn J. N., Holman M. J., 2008, ApJ, 677, 1324

Traub W. A., Oppenheimer B. R., 2010, Direct Imaging of Exoplanets. pp 111–156

Tregloan-Reed J., et al., 2015, MNRAS, 450, 1760

Triaud A. H. M. J., 2014, MNRAS, 439, L61

Triaud A. H. M. J., et al., 2010, A&A, 524, A25

Triaud A. H. M. J., et al., 2013, A&A, 551, A80

Triaud A. H. M. J., Lanotte A. A., Smalley B., Gillon M., 2014, MNRAS, 444, 711

Triaud A. H. M. J., et al., 2015, MNRAS, 450, 2279

Turner J. D., et al., 2016, MNRAS, 459, 789

Venot O., Cavalié T., Bounaceur R., Tremblin P., Brouillard L., Ben Lhoussaine Brahim R., 2019, arXiv e-prints, p. arXiv:1912.07246

Visscher C., Lodders K., Fegley Bruce J., 2006, ApJ, 648, 1181

Wakeford H. R., et al., 2018, AJ, 155, 29

Waldmann I. P., Rocchetto M., 2015, in AAS/Division for Extreme Solar Systems Abstracts. p. 119.20

Wallack N. L., et al., 2019, arXiv e-prints, p. arXiv:1908.00014

Wang W., van Boekel R., Madhusudhan N., Chen G., Zhao G., Henning T., 2013, ApJ, 770, 70

Wang D., Miguel Y., Lunine J., 2017, ApJ, 850, 199

Wang Y.-H., et al., 2019, AJ, 157, 82

West R. G., et al., 2016, A&A, 585, A126

Wheatley P. J., et al., 2010, arXiv e-prints, p. arXiv:1004.0836

Wilson D. M., et al., 2008, ApJ, 675, L113

Winn J. N., 2010, Exoplanet Transits and Occultations. pp 55–77

Winn J. N., et al., 2010, ApJ, 718, 575

Wolszczan A., Frail D. A., 1992, Nature, 355, 145

Wong I., et al., 2014, ApJ, 794, 134

Wong I., et al., 2016, ApJ, 823, 122

Wright J. T., 2018, Radial Velocities as an Exoplanet Discovery Method. p. 4, doi:10.1007/978-3-319-55333-7_4

Wright J. T., Gaudi B. S., 2013, Exoplanet Detection Methods. p. 489, doi:10.1007/978-94-007-5606-9_10

Yee S. W., et al., 2020, ApJ, 888, L5

Zahnle K. J., Marley M. S., 2014, ApJ, 797, 41

Zellem R. T., et al., 2014, ApJ, 790, 53

Zhao M., Monnier J. D., Swain M. R., Barman T., Hinkley S., 2012, ApJ, 744, 122

Zhao M., et al., 2014, ApJ, 796, 115

Zhou G., Bayliss D. D. R., Kedziora-Chudczer L., Salter G., Tinney C. G., Bailey J., 2014, MNRAS, 445, 2746

Zhou G., Bayliss D. D. R., Kedziora-Chudczer L., Tinney C. G., Bailey J., Salter G., Rodriguez J., 2015, MNRAS, 454, 3002

de Mooij E. J. W., de Kok R. J., Nefs S. V., Snellen I. A. G., 2011, A&A, 528, A49

de Mooij E. J. W., Brogi M., de Kok R. J., Snellen I. A. G., Kenworthy M. A., Karjalainen R., 2013, A&A, 550, A54